

Manuscript Number: LITHOS8642R1

Title: Mineralogy of the HSE in the Subcontinental Lithospheric Mantle – an interpretive review

Article Type: VSI:SCLM GONZÁLEZ

Keywords: Sulfides; platinum-group minerals; nanoparticles;
Subcontinental Lithospheric Mantle; partial melting; metasomatism

Corresponding Author: Dr. JOSÉ MARÍA Maria GONZÁLEZ-JIMÉNEZ, Dr

Corresponding Author's Institution: Universidad de Granada

First Author: JOSÉ MARÍA Maria GONZÁLEZ-JIMÉNEZ, Dr

Order of Authors: JOSÉ MARÍA Maria GONZÁLEZ-JIMÉNEZ, Dr; Santiago Tassara, Dr.; Erwin Schettino, Msc; Josep Roqué-Rosell, Dr.; Julia Farré-de-Pablo, Msc; Edward Saunders, Dr.; Artur P Deditius, Dr.; Vanessa Colás; Juan J. Rovira-Medina, Msc; Maria Guadalupe Dávalos, Dr.; Manuel Schilling, Dr.; Abigail Jiménez-Franco, Dr.; Claudio Marchesi, Dr.; Fernando Nieto, Dr.; Joaquín A Proenza, Dr.; Fernando Gervilla, Dr.

Abstract: The highly siderophile elements (HSE: Os, Ir, Ru, Rh, Pt, Pd, Re, Au) exist in solid solution in accessory base-metal sulfides (BMS) as well as nano-to-micron scale minerals in rocks of the subcontinental lithospheric mantle (SCLM). The latter include platinum-group minerals (PGM) and gold minerals, which may vary widely in morphology, composition and distribution. The PGM form isolated grains often associated with larger BMS hosted in residual olivine, located at interstices in between peridotite-forming minerals or more commonly in association with metasomatic minerals (pyroxenes, carbonates, phosphates) and silicate glasses in some peridotite xenoliths. The PGM found inside residual olivine are mainly Os-, Ir- and Ru-rich sulfides and alloys. In contrast, those associated with metasomatic minerals or silicate glasses of peridotite xenoliths consist of Pt, Pd, and Rh bonded with semimetals like As, Te, Bi, and Sn. Nanoscale observations on natural samples along with the results of recent experiments indicate that nucleation of PGM is mainly related with the uptake of HSE by nanoparticles, nanominerals or nanomelts at high temperature (> 900 °C) in both silicate and/or sulfide melts, regardless of the residual or metasomatic origin of their host minerals. A similar interpretation can be assumed for gold minerals, whose formation is exclusively related to metasomatic BMS. Our observations highlight that nanoscale processes play an important role on the ore-forming potential of primitive mantle-derived magmas parental to magmatic-hydrothermal deposits enriched in noble metals. The metal inventory in these magmas could be related with the physical incorporation of HSE-nanoparticles (HSE-NPs) during processes of partial melting of mantle peridotite and melt migration from the mantle to overlying continental crust.

1 **Mineralogy of the HSE in the Subcontinental** 2 **Lithospheric Mantle —an interpretive review**

3

4

5 José M. González-Jiménez^a, Santiago Tassara^b, Erwin Schettino^c, Josep Roqué-
6 Rosell^d, Julia Farré-de-Pablo^d, J. Edward Saunders^e, Artur P. Deditius^f, Vanessa
7 Colás^g, Juan J. Rovira-Medina^a, María Guadalupe Dávalos^h, Manuel Schillingⁱ,
8 Abigail Jimenez-Franco^{d,j}, Claudio Marchesi^{a,c}, Fernando Nieto^{a,c}, Joaquín A.
9 Proenza^e, Fernando Gervilla^{a,c}

10

- 11 a. Departamento de Mineralogía y Petrología, Facultad de Ciencias, Universidad de
12 Granada, Avda. Fuentenueva s/n, 18002 Granada, Spain.
- 13 b. Department of Earth and Planetary Sciences, Yale University, New Haven,
14 Connecticut 06511, USA.
- 15 c. Instituto Andaluz de Ciencias de la Tierra (IACT), CSIC-UGR, Avda. de las
16 Palmeras 4, 18100 Armilla, Granada, Spain.
- 17 d. Departament de Mineralogia, Petrologia i Geologia Aplicada, Facultat de Ciències de
18 la Terra, Universitat de Barcelona, 08028 Barcelona, Spain.
- 19 e. Division of Earth Sciences, School of Environmental and Rural Science, University
20 of New England, Armidale NSW 2351, Australia.
- 21 f. Discipline of Chemistry and Physics, College of Science, Health, Education and
22 Environment (CSHEE), Murdoch University, Murdoch, 6150 WA, Australia.
- 23 g. Instituto de Geología, Universidad Nacional Autónoma de México, Ciudad
24 Universitaria, 04510 Ciudad de México, Mexico.
- 25 h. Facultad de Ciencias, Universidad Nacional Autónoma de México, Ciudad
26 Universitaria, 04510 Ciudad de México, Mexico.
- 27 i. Instituto de Ciencias de la Tierra, Universidad Austral de Chile, Valdivia 5090000,
28 Chile
- 29 j. Posgrado en Ciencias de la Tierra, Universidad Nacional Autónoma de México,
30 Ciudad Universitaria, Delegación Coyoacán, 04510 Cd. de México, Mexico.

31

32

Submitted to Lithos Special Issue

33

“Origin and Evolution of Continental Mantle Lithosphere and its Resource Endowment”

34

35

36

*Corresponding author: José María González Jiménez

37

Address: Departamento de Mineralogía y Petrología, Facultad de Ciencias, Universidad de Granada,
38 Granada, Spain

39

Avda. Fuentenueva s/n 18002 Granada

40

Phone: +34 958 24 66 19

41

E-mail: jmgonzj@ugr.es

42

43 **Abstract**

44 The highly siderophile elements (HSE: Os, Ir, Ru, Rh, Pt, Pd, Re, Au) exist in
45 solid solution in accessory base-metal sulfides (BMS) as well as nano-to-micron scale
46 minerals in rocks of the subcontinental lithospheric mantle (SCLM). The latter
47 include platinum-group minerals (PGM) and gold minerals, which may vary widely in
48 morphology, composition and distribution. The PGM form isolated grains often
49 associated with larger BMS hosted in residual olivine, located at interstices in
50 between peridotite-forming minerals or more commonly in association with
51 metasomatic minerals (pyroxenes, carbonates, phosphates) and silicate glasses in
52 some peridotite xenoliths. The PGM found inside residual olivine are mainly Os-, Ir-
53 and Ru-rich sulfides and alloys. In contrast, those associated with metasomatic
54 minerals or silicate glasses of peridotite xenoliths consist of Pt, Pd, and Rh bonded
55 with semimetals like As, Te, Bi, and Sn. Nanoscale observations on natural samples
56 along with the results of recent experiments indicate that nucleation of PGM is mainly
57 related with the uptake of HSE by nanoparticles, nanominerals or nanomelts at high
58 temperature (> 900 °C) in both silicate and/or sulfide melts, regardless of the residual
59 or metasomatic origin of their host minerals. A similar interpretation can be assumed
60 for gold minerals, whose formation is exclusively related to metasomatic BMS. Our
61 observations highlight that nanoscale processes play an important role on the ore-
62 forming potential of primitive mantle-derived magmas parental to magmatic-
63 hydrothermal deposits enriched in noble metals. The metal inventory in these magmas
64 could be related with the physical incorporation of HSE-nanoparticles (HSE-NPs)
65 during processes of partial melting of mantle peridotite and melt migration from the
66 mantle to overlying continental crust.

67

68 **Keywords:** Sulfides, platinum-group minerals, nanoparticles, Subcontinental Lithospheric
69 Mantle, partial melting, metasomatism

70 **1. Introduction**

71 The highly siderophile elements (HSE), also known as the noble or precious
72 metals, include the six platinum-group elements (PGE: Os, Ir, Ru, Rh, Pt, Pd) along
73 with Re and Au. Experimental studies have shown that these transition metals have a
74 strong affinity for iron (siderophile affinity) as reflected in their high (10^5 - 10^8)

75 metal/silicate melt partition coefficients over a large range of temperature and
76 pressure conditions (e.g., [Mann et al., 2012](#); [Brenan et al., 2016](#)). However,
77 observations on natural mantle rocks show that the inventory of the HSE in the
78 Earth's upper mantle is mostly stored in accessory (< 1 % modal) base-metal sulfides
79 (BMS) of the Ni-Fe-Cu system rather than alloys ([Luguet and Reisberg, 2016](#)),
80 revealing that they are both siderophile and chalcophile elements in nature. This is
81 because most of terrestrial magmatic systems are relatively oxidized (above the iron-
82 wustite buffer), such that native Fe is not stable. Consequently, the HSE also display
83 very high partition coefficients for sulfide in magmatic systems (e.g., [Li and Audétat,](#)
84 [2013](#); [Mungall and Brenan, 2014](#)).

85 In the Earth's upper mantle, the HSE may also form their own minerals
86 essentially constituted by PGE, which are known as as platinum-group minerals
87 (PGM). The latter may include alloys, sulfides, arsenides, sulfarsenides, tellurides,
88 bismuthides, or stannides ([O'Driscoll and González-Jiménez, 2016](#) and references
89 therein). Most of our knowledge of the variety and distribution of the PGM in the
90 upper mantle comes from the study of chromite-rich rocks (i.e., chromitites) hosted in
91 mantle peridotites from ophiolite complexes. In this setting, the PGM form by both
92 magmatic (i.e., primary) and post-magmatic (i.e., secondary related to
93 serpentinization, hydrothermal alteration, metamorphism and weathering) processes
94 ([O'Driscoll and González-Jiménez, 2016](#)).

95 In the field of SCLM research, the mineralogy of the HSE is only recently
96 beginning to receive the attention it deserves, very likely reflecting the fact that most
97 of previous studies had focused their effort on the analysis of HSE apparently
98 dissolved in solid solution in the BMS (e.g., [Luguet and Reisberg, 2016](#)). Although
99 knowledge on the mineralogy of HSE in the SCLM is available from the study
100 peridotite massifs cropping out in the French Pyrenees (e.g., [Luguet et al., 2007](#);
101 [Lorand et al., 2010](#); [Ferraris and Lorand, 2015](#)), minerals of the HSE have been
102 generally overlooked on other peridotite samples from the SCLM such as ultramafic
103 xenoliths. Of particular importance are the recent studies showing the existence of
104 nano-sized PGM and gold particles in peridotite xenoliths from both cratonic
105 ([Wainwright et al., 2016](#)) and off-craton regions ([Tassara et al., 2017](#); [González-](#)

106 [Jiménez et al., 2019](#)). These new advances suggest a critical role of nanoscale
107 processes in controlling HSE fractionation, transport and concentration in the SCLM.

108 This paper provides a state-of-the-art review of the mineralogy of the HSE, at
109 the nano- and micron-scales, in different rock suites of the SCLM. Our main purpose
110 is to foster the debate about the origin of these minerals in rocks from the SCLM and
111 its potential implications for our understanding of HSE geochemical behavior in the
112 upper mantle. To achieve this goal, we focus on ultramafic xenoliths and mineral
113 xenocrysts hosted in off/on craton volcanic rocks as well as on exhumed fragments of
114 the SCLM (i.e., orogenic peridotites) ranging in age from Archean to Quaternary ([Fig.](#)
115 [1](#) and [Appendix 1](#)). Furthermore, in order to provide an up-to-date picture of the
116 origin of HSE-bearing minerals in the SCLM, we also compare the different genetic
117 models proposed in the literature, taking into account the microstructural location of
118 the minerals. Our interpretive review is based on the integration of information
119 acquired from the pre-existing literature with our novel research, with a strong
120 emphasis on the new results provided by using a combination of focused ion beam
121 and high-resolution transmission electron microscopy (FIB/HRTEM). The focused
122 ion beam (FIB) tool has been successfully used to prepare site-specific electron
123 transparent thin foils from minerals, which enables high-resolution (cross-section)
124 imaging by high-resolution transmission electron microscopy (HRTEM). The
125 combination of FIB and scanning-electron microscopy (SEM) methods applied to
126 minerals represent an in-situ approach for sample characterization and thus provides
127 relevant crystal–chemical data that can be placed into the geological context ([Wirth,](#)
128 [2004, 2009](#); [Lee, 2010](#); [Ciobanu et al., 2011](#); [Wirth et al., 2013](#); [Junge et al., 2015](#)).

129 **2. Previous reports of HSE-bearing nano and micron-sized minerals** 130 **in the subcontinental lithospheric mantle**

131 *2.1. Off-craton peridotite xenoliths*

132 The first ever PGM reported on rocks from the SCLM are two grains (~500
133 nm) of cooperite (PtS) and paalovite (Pd₂Sn), which were found in partly desulfurized
134 pentlandite blebs hosted in olivine and metasomatic pyroxene, respectively, within
135 lherzolite xenoliths from the SCLM beneath Mount Porndon in southeastern Australia
136 ([Fig. 1](#); [Keays et al., 1981](#)). According to [Keays et al. \(1981\)](#) the PGM exsolved at

137 low temperatures (<300 °C) from pentlandite formed by the breakdown of former Fe-
138 Ni monosulfide solid solution (MSS).

139 Several decades later, [Wang et al. \(2009\)](#) discovered Pt-rich micronuggets in
140 Fe-rich MSS in non-cratonic peridotite nodules from the Penghu Islands, Taiwan (Fig.
141 1). The nuggets were identified as sharp spikes in the Pt signal of the time-resolved
142 LA-ICP-MS spectra, although they could not firmly confirm the nature of PGM by
143 other analytical techniques.

144 [Alard et al. \(2011\)](#) and [Depelch et al. \(2012\)](#) also identified several grains of
145 Pt-Te-Bi and f Pt-Pd-As (including sperrylite PtAs₂) in spinel-peridotite xenoliths
146 from Montferrier (Languedoc, France, [Fig. 1](#)) and in dunite xenoliths from the
147 Kerguelen Archipelago (France, [Fig. 1](#)). These PGM were associated with
148 pentlandite-chalcopyrite (\pm cubanite) blebs coexisting with interstitial metasomatic
149 carbonates, and were detected on both on polished thin sections and during *in situ*
150 LA-ICPMS analysis. [Alard et al. \(2011\)](#) and [Depelch et al. \(2012\)](#) suggested that Pt-
151 bismuthotellurides formed by fractional crystallization of a Cu-Ni-rich sulfide melt
152 whereas Pt-Pd-rich arsenides crystallized at temperatures below or near 900°C (i.e.,
153 below the solidus of the sulfide) by the reaction of sulfide-hosted Pt-
154 bismuthotellurides with volatile-rich fluids that refertilized the SCLM.

155 Other PGM found in off-craton peridotite xenoliths include Pt-alloys reported
156 by [O'Driscoll and González-Jiménez \(2016\)](#) associated with Fe-rich MSS located at
157 olivine interstices in lherzolite xenolith from the Calatrava Volcanic Field, central
158 Spain ([Fig. 1](#)). [González-Jiménez et al. \(2019\)](#) also reported nanometer-sized (< 100
159 nm) grains of hongshiite (PtCu) and tulameenite (Pt₂CuFe) hosted in pentlandite
160 embedded in metasomatic silicate glasses from mantle lherzolite xenoliths from Cerro
161 Redondo and Gobernador Gregores in southern Patagonia. [González-Jiménez and co-
162 workers \(2019\)](#) suggested that these Pt-rich nanoalloys as well as other nanometer-
163 sized Pt-rich arsenides that were found in these interstitial glasses, could have
164 segregated earlier, either directly from the infiltrating alkaline basaltic melt prior to
165 sulfide saturation in the silicate melt, or from droplets of immiscible sulfide melt once
166 sulfide saturation was achieved. [Tassara et al. \(2017\)](#) proposed a similar
167 interpretation to explain the origin of gold particles (< 2µm) embedded in interstitial
168 metasomatic silicate glass veins and associated BMS (millerite and chalcopyrite) also

169 found in lherzolite xenolith from Cerro Redondo. Finally, [Mundl et al., \(2015\)](#)
170 identified a micron-sized grain of laurite (RuS₂) at the boundary between metasomatic
171 clinopyroxene and orthopyroxene in a harzburgitic xenolith from Puesto Díaz in the
172 North Patagonian Massif. These authors suggested that laurite could have precipitated
173 from a sulfur-undersaturated metasomatic silicate melt percolating by porous flow
174 through the SCLM, although they did not explain the specific mechanism accounting
175 for laurite crystallization.

176 *2.2. Peridotite xenoliths and olivine xenocrysts sampling SCLM in cratonic regions*

177 Several PGM grains have been detected within mantle xenolith samples of the
178 SCLM in cratonic regions, including ([Fig. 1](#)): (1) micron-sized Pt-Ir-Os in MSS
179 grains enclosed in olivine crystals from mantle peridotites trapped by the Udachnaya
180 kimberlite (Siberian craton; [Griffin et al., 2002](#)), (2) Pt-rich sulfide grains (possibly
181 cooperite, PtS) in lherzolite xenoliths collected from the cratonic Hebridean Terrane
182 (localities of Loch Roag and Rinibar) in the northwest Scotland ([Hughes et al., 2016](#)),
183 and (3) micron-sized Pt-Fe (\pm Ir-Rh) alloys included in two pentlandite grains from a
184 single cratonic harzburgite sampled by the Bultfontein kimberlite (Kaarvaal craton,
185 South Africa; [Wainwright et al., 2016](#)).

186 [Griffin et al. \(2002\)](#) identified the Pt-Ir-Os alloys by inspecting the time-
187 resolved signals collected during LA-ICP-MS. These authors suggested a residual
188 origin for these alloys as a result of small degrees of partial melting of a pre-existing
189 BMS in a mantle region under sulfur undersaturated conditions. The cooperite grains
190 reported by [Hughes et al. \(2016\)](#) were observed within the chalcopyrite portion of a
191 composite sulfide (pyrrhotite-pentlandite-chalcopyrite)-carbonate bleb, along the
192 margin with pyrrhotite. The composite sulfide assemblage was interstitially located
193 between primary silicates of the peridotitic matrix, and interpreted to have formed
194 upon cooling of a sulfide liquid. In Bultfontein xenoliths, PGM alloys were detected
195 as pentlandite-hosted inclusions in composite sulfide grains (pyrrhotite + pentlandite).
196 Composite sulfides were observed as inclusions located at the contact between partly
197 serpentinized olivine and the interstitial medium, either enclosed (along with
198 phlogopite) within metasomatic clinopyroxene. The FIB-TEM characterization on
199 thin foils indicates that PGM alloys (<1 μ m long and ~75 nm width) in olivine-hosted
200 blocky pentlandite were misoriented relative to the sulfide matrix. On the other hand,

201 PGM (1-5 μm long and <500 nm width) found in the clinopyroxene-hosted
202 pentlandite formed oriented lamellae within the sulfide matrix. According to
203 [Wainwright et al. \(2016\)](#) the two distinct BMS, as well as their Pt–Fe-alloy
204 inclusions, represent different stages of a single sequence of fractional crystallization
205 and subsolidus re-equilibration of a Ni-rich sulfide matte, with the blocky pentlandite
206 and Pt–Fe-alloys having crystallized at higher temperature (i.e., 760 °C) relative to the
207 pentlandite-pyrrhotite exsolution and their numerous texturally aligned Pt–Fe-alloys
208 (<610 °C).

209 2.3. Exhumed ultramafic massifs

210 HSE-bearing minerals reported on peridotite samples from the SCLM
211 exhumed in orogenic belts (i.e., orogenic peridotite massifs) include: (1) an euhedral
212 (cubic) inclusion of Pt-Fe-Ni (87.0 wt.% Pt, 11.2 wt.% Fe and 2.22 wt.% Ni) about 6
213 x 5 μm in size within a pentlandite grain interstitial to primary silicates on a lherzolite
214 sample from Balmuccia (Ivrea Complex, northern Italy) ([Garuti et al., 1984](#)), (2) a
215 grain of moncheite (PtTe_2) $< 2\mu\text{m}$ within olivine-hosted pentlandite from a spinel-
216 bearing clinopyroxenite dyke from the Ronda massif in southern Spain ([Fig. 1](#);
217 [Gutiérrez-Narbona, 1999](#)), and (3) several (>100 grains) PGM and gold minerals from
218 the Lherz massif and its cluster of peridotite outcrops (Ariège, Freychinède, Fontête
219 Rouge) in the French Pyrenees ([Fig. 1](#); [Luguet et al., 2007](#); [Lorand et al., 2010](#);
220 [Köning et al., 2015](#)). The suite of HSE-bearing minerals identified in the French
221 ultramafic massifs include micron to submicron grains of Ru-Os sulfides [members of
222 the laurite (RuS_2)-erlichmanite (OsS_2) solid solution series], Pt-Ir-Cu \pm Rh sulfides
223 [members of the malanite (CuPt_2S_4)- cuproiridsite (CuIr_2S_4) solid solution series,
224 braggite (PdNiS)], Pt-Pd-Te-Bi minerals [moncheite (PtTe_2) –merenskyite (PdTe_2)],
225 sperrlyite (PtAs_2), as well as Pt-Ir \pm (Os) alloys, and an unidentified Pd-Cu mineral.
226 All these PGM were systematically associated with BMS, and were detected on
227 polished thin sections and during *in situ* LA-ICPMS analysis of BMS ([Lorand et al.,](#)
228 [2010](#)), as well as by X-ray micro-CT scanning of the peridotite samples ([ning et al.,](#)
229 [2015](#)). Most of BMS were located along mineral grain boundaires of the peridotite
230 matrix, or enclosed in olivine crystals, except one grain of pure platinum included
231 within a Cr-spinel grain. Laurite-erlichmanite and Pt–Ir–Os alloys were interpreted as
232 refractory minerals formed after partial melting (20-30%) of a former MSS, very

233 likely prior to the complete consumption of the MSS (Luguet et al., 2007; Köning et
234 al., 2015). According to Lorand et al. (2010) such formation of the PGM as residual
235 phases might be attributed to a series of partial melting events in the (~2 Ga) SCLM,
236 which removed the BMS and left refractory PGM as stable minerals under S-
237 undersaturated conditions. In contrast, the minerals of the malanite-cuproiridite solid
238 solution series, sperrylite and the Pt-Pd-Te-Bi system were interpreted to have formed
239 via subsolidus re-equilibration of S- and Cu-rich, volatile-rich, small melt fractions
240 that metasomatized the Lherz SCLM.

241 Lorand et al. (2010) also noted that the peridotite sample hosting PGM in
242 Lherz contain micron-sized grains of native gold, which were observed filling
243 fractures or close to the altered contact between chalcopyrite and pentlandite. A few
244 years later, Ferraris and Lorand (2015) identified micrometric inclusions of
245 novodneprite (AuPb_3), anyuiite [$\text{Au}(\text{Pb},\text{Sb})_2$] and nanometric clusters of gold in
246 olivine grains of these peridotites using HRTEM and electron energy loss
247 spectroscopy (EELS). According to these authors, novodneprite and anyuiite formed
248 during subsolidus recrystallization of the Pyrenean lherzolites following the growth of
249 secondary olivine that trapped inter-granular components Ductile deformation likely
250 triggered the formation of dislocations within the olivine grains and enhanced the
251 circulation of metasomatic Au-enriched fluids.

252 The coexistence of PGM and gold was also reported in a spinel lherzolite from
253 the Horoman peridotite complex (Japan) (Fig. 1). In this sample from the SCLM,
254 Kogiso et al. (2008) identified nine grains of PGM alloys (~1 to 10 μm), including
255 Os-Ir, Os-Ir-Pt, Pt-Bi Pt-Au, Pt, and Au, using microbeam synchrotron radiation X-
256 ray fluorescence analysis. All these grains were located near, or within, pentlandite
257 grains interstitially distributed among primary olivine and pyroxene However, no
258 explanation for the origin of these PGM and gold minerals was provided.

259 **3. New discoveries of PGM and gold minerals and nanoparticles in** 260 **SCLM xenoliths**

261 In the present study, we describe new nano- and micron-sized minerals and
262 particles of the HSE in different microtextural locations within SCLM xenoliths
263 (lherzolites and harzburgites) from on/off-craton regions. The samples background the

264 analytical procedures used to characterize their HSE-bearing minerals are provided in
265 [Appendix 1](#) and [2](#), respectively.

266 *3.1. Pt-Fe alloys and laurite in base-metal sulfide blebs enclosed in residual olivine*

267 We found PGE-rich nanoparticles enclosed within a composite sulfide
268 aggregate consisting of monoclinic Ni-rich pyrrhotite (see below) and pentlandite,
269 which is hosted in a residual olivine grain from a peridotite xenolith from Tres Lagos
270 (southern Patagonia; sample TL-2-1) ([Fig. 2A-G](#); [Appendix 3-5](#)). The obtained field
271 emission scanning electron microscopy (FESEM) and energy dispersive spectra
272 (EDS) ([Appendix 4](#)) revealed two types of nanoparticles consisting of Pt-Fe and Ru-
273 Os-S. However, many of these minerals were too small for reliable identification
274 and/or quantitative analyses.

275 The FIB thin-foil cut through the contact between the pyrrhotite and
276 pentlandite crystals intersected three of these PGE-rich nanoparticles ([Fig. 3](#)). Two of
277 the nanoparticles (A and C in [Fig. 4](#)) are enclosed in pyrrhotite whereas the third
278 nanoparticle (B in [Fig. 4](#)) was found in pentlandite ([Fig. 4A-C](#)). The longest
279 dimension of the nanoparticles is ~500 nm. The high-angle annular dark-field
280 (HAADF) images obtained by means of HRTEM for all these nanoparticles show that
281 they are homogenous crystals containing rounded inclusions (<30 nm) of a Fe-O
282 compound ([Fig. 4A-C](#)). The corresponding fast Fourier transform (FFT) patterns
283 allow us to identify these crystalline nanoparticles as laurites (RuS₂) embedded in a
284 distinctly oriented matrix of a defective monoclinic pyrrhotite and pentlandite ([Fig.](#)
285 [5A-C](#); [Appendix 5](#)). Laurite grains are characterized internally by a compositional
286 core-to-rim Os enrichment ([Fig. 4A-C](#); i.e., normal zoning as defined by [González-](#)
287 [Jiménez et al. \(2009\)](#) for members of the laurite [RuS₂]-erlichmanite [OsS₂] solid
288 solution series). The nanostructural analysis of one of the rounded FeO compounds
289 (particle enclosed in the dotted rectangles B3 shown in [Fig 5](#)) reveals a well-
290 crystallized magnetite (with the corresponding d-spacing (400) at 2.09 Å) with no
291 crystallographic continuity relative to its laurite host (d-spacing (111) at 3.2 Å)
292 ([Appendix 5](#)). In addition, the analysis of the HRTEM images and FFT indicates the
293 presence of irregular contacts and crystal misorientations between pyrrhotite and
294 pentlandite even at the nanoscale ([Figs. 3 and 5](#)).

295 3.2. *Native Pt, Pt-rich tellurides and stannides associated with base-metal sulfides in*
296 *metasomatic pyroxenes*

297 Base-metal sulfides hosted in metasomatic clinopyroxenes from Tres Lagos
298 (southern Patagonia; sample PM-11) contain submicron (~500 nm to ~2µm) crystals
299 of native platinum (Fig. 6A, A1 and A2; Appendix 3-4). Noteworthy, these nano-
300 PGM are located at the margin of the chalcopyrite portion of the sulfide globule,
301 which consists of a polyphase assemblage made up of Ni-rich pyrrhotite, pentlandite
302 and chalcopyrite.

303 Two grains of a Pt-Te mineral (possibly moncheite, PtTe₂) of <2 µm in
304 diameter were identified in a xenolith collected from southern Patagonia at the
305 eruptive center of Cerro Redondo (Fig. 6B; sample CR-01). Both grains were
306 associated with pentlandite and located in the core of the sulfide or along the contact
307 with chalcopyrite.

308 Metasomatic clinopyroxene and orthopyroxene from mantle xenoliths of
309 Tallante (eastern Betics, southeast Spain) contain pentlandite blebs hosting nano-to-
310 micro (<1.5 µm in diameter) particles of a Pt-Sn mineral (Fig. 6C-E; Appendix 3-5).
311 These grains exhibit euhedral morphologies and are commonly located at the margin
312 of pentlandite grains in contact with a silicate melt inclusion (Fig. 6C) or chalcopyrite
313 (Fig. 6E), either enclosed within pentlandite (Fig. 6D). A FIB section of the Pt-Sn
314 particle shown in Fig. 6E-1 reveals euhedral shape with sharp contacts with
315 pentlandite, magnetite and chalcopyrite (Fig. 7-9). The magnetite is located between
316 Pt-Sn and chalcopyrite. The TEM-EDS elemental mapping of the Pt-Cu-Sn particle
317 shows homogeneous distribution of Pt, Cu, Sn and Pd (Fig. 8). The FFT analysis of
318 the HRTEM images of the associated minerals revealed that pentlandite, magnetite,
319 and tatyanaite [ideally (Pt₉Cu₃Sn₄) are single crystals. Tatyanaite was identified based
320 on the corresponding d-spacing (100) at 2.30 Å. There is lack of crystallographic
321 continuity between tatyanaite and host pentlandite and associated magnetite (Fig. 9;
322 Appendix 5).

323 3.3. *Nanoparticles of Pt-Pd ± S ± Te ± As and laurite in silicate glasses and*
324 *associated base-metal sulfides*

325 Pt-rich (<1µm) particles occur as pentlandite-hosted inclusions embedded

326 within interstitial silicate glass in xenoliths from Gobernador Gregores in Patagonia
327 (Fig. 10A; replicates of the sample GG-14 analyzed by González-Jiménez et al.,
328 2019) as well as in xenoliths from La Breña in Central Mexico (Fig. 10B-C; samples
329 LB-1 and LB-3). Some of these pentlandite grains are frequently altered to oxy-
330 hydroxides.

331 Other pentlandite blebs entrained in the interstitial glass of xenoliths from
332 southern Patagonia contain Pd-rich minerals, including: (1) Pd-S (possibly braggite,
333 PdS) located at the contact between pyrrhotite and pentlandite from a xenolith oin
334 Gobernador Gregores (Fig. 10D; sample GG-01), and (2) Pd-Te (possibly
335 merenskyite, PdTe₂) and Pt-As (possibly sperrylite PtAs₂) found at the grain
336 boundaries between pentlandite and millerite in the xenoliths from Cerro Redondo
337 (Figs 10E-G; replicates of samples CR-08 studied by Tassara et al., 2017).

338 Two grains of a Ru-S mineral (possibly laurite, RuS₂) were observed within
339 the interstitial glass in samples from southern Patagonia in the localities of Cerro
340 Redondo (sample CR-08) and Pali-Aike (sample PA-LA7) (Figs. 10I-J).

341 3.4. Gold

342 We have identified nanometer-sized particles of native gold in droplet-shaped
343 inclusions of pentlandite grains, which are hosted in metasomatic clinopyroxenes
344 from the Tallante xenoliths in southern Spain (Fig. 11A-B and Appendix 6; samples
345 TAL-110, TAL-129). Moreover, native gold was also observed within the
346 chalcopyrite portion of composite pentlandite-chalcopyrite aggregates entrained in the
347 interstitial glass of southern Patagonian xenoliths (Fig. 11C-D and 12; sample CR-08
348 studied by Tassara et al., 2017). Nanoparticles of gold, often coexisting with Pt, are
349 also common in partly altered pentlandite droplets in the interstitial glass of mantle
350 xenoliths from La Breña in Central Mexico (Fig. 11E-G; samples LB-1 and LB-3).

351 In addition, a re-examination of the time-resolved data acquired during LA-
352 ICP-MS analysis of sulfides hosted in metasomatized spinel lherzolites from Svalbard
353 (Saunders et al., 2015) and garnet lherzolites and harzburgites from Kaapvaal (Griffin
354 et al., 2004) has revealed the presence of several micron-sized nuggets of gold in
355 BMS (Appendix 6). These BMS consisting of MSS or pentlandite are also associated
356 with metasomatic silicate glasses or pyroxene.

357 4. Discussion

358 4.1. The origin of nano-PGM associated with BMS included in residual olivine

359 The BMS grain from Tres Lagos shown in Figs. 2-5 exhibits a droplet-shaped
360 morphology without any evidence to be related with visible fractures or a trail of
361 secondary inclusions. These microstructural features in mantle sulfides are interpreted
362 as an evidence of former immiscible sulfide melt droplet mechanically trapped by
363 growing olivine (e.g., Andersen et al., 1987; Szabó and Bodnar, 1995). This inclusion
364 consists of Ni-rich pyrrhotite and pentlandite, indicating that even though the
365 immiscible sulfide melts were segregated before or contemporaneously to olivine
366 crystallization at $>1000^{\circ}\text{C}$ (Tassara et al., 2018), the observed sulfide assemblage is
367 not primary owing to the lower thermal stability of pentlandite ($< 870^{\circ}\text{C}$; Sugaki and
368 Kitakaze, 1998; Kitakaze et al., 2016). The irregular contacts between pyrrhotite and
369 pentlandite at the micron (Fig. 2) and nanoscale (Fig. 3), as well as the different
370 orientation of their crystal lattice, may suggest the possible formation of pentlandite
371 by a peritectic reaction of MSS crystallites (now represented by Ni-rich pyrrhotite)
372 with a Ni-richer melt (e.g., Sugaki and Kitakaze, 1998; Kitakaze et al., 2016).
373 However, the reconstructed composition of the original sulfide (Appendix 4) falls
374 within the mixing line between the measured composition of pyrrhotite and
375 pentlandite. This suggests that Ni was not additionally added to the system as would
376 be expected if a peritectic reaction formed pentlandite. Therefore, these micro- and
377 nano-structural relationships simply reflect the low temperature exsolution of granular
378 and flame-like pentlandite at $<610^{\circ}\text{C}$, from re-equilibrating MSS.

379 The residual nature of the host olivine links the origin of this BMS grain with
380 partial melting events experienced by the host rock (Alard et al., 2002). Experimental
381 (Peregoedova et al., 2004; Bockrath et al., 2004a; Fonseca et al., 2012) and empirical
382 (Luguet et al., 2007; Barnes et al., 2016) results show that variable rates of partial
383 melting of BMS under decreasing $f\text{S}_2$ at $\geq 1000^{\circ}$ may result in the formation of Os, Ir,
384 Ru and Pt enriched residual Fe-rich MSS with coexisting Ni-richer melts/solids ($<$
385 10% partial melting) or PGM (laurite, Os-Ir-Ru or Pt-Fe alloys; 10-20% partial
386 melting). In this scenario, nano-sized laurite grains enclosed in both pyrrhotite and
387 pentlandite (Figs. 2 and 3) may be interpreted as the result of high-temperature
388 exsolution during partial melting and desulfurization of MSS (e.g., Peregoedova et al.,

389 [2004](#); [Luguet et al., 2007](#); [Barnes et al., 2016](#)). However, this interpretation is
390 inconsistent with: (1) the well-crystallized nature of laurite, distinctively different
391 from the defective lattice of pyrrhotite, (2) the lack of crystallographic continuity
392 between laurite grains and their host pyrrhotite and pentlandite crystals, (3) the
393 normal zoning of laurite, and (4) the presence of drop-like inclusions of magnetite
394 within laurite. Alternatively, all these observation are at odds for crystallization of
395 laurite from melt.

396 Experimental studies indicate that laurite can crystallize directly out from Ni-
397 rich sulfide melts before the crystallization of a MSS ([Sinyakova et al., 2019](#)),
398 consistent with its elevated solidus temperature (>1110-1200 °C) in the Ni-Fe-Cu
399 system ([Brenan and Andrews, 2001](#); [Andrews and Brenan, 2002](#)). Moreover, the
400 normal zoning exhibited by laurite grains (i.e., Os enrichment towards the rim [Fig. 4](#))
401 suggests their crystallization from a cooling S-poor melt ([González-Jiménez et al.,](#)
402 [2009](#)). This melt was also able to crystallize Pt-Fe alloys, such as those observed in
403 several experimental works ([Fleet and Stone, 1991](#); [Peregoedova and Ohnenstetter,](#)
404 [2002](#); [Peregoedova et al., 2004](#); [Fonseca et al., 2017](#)).

405 Besides, the rounded morphology of magnetite inclusions along with the lack
406 of crystallographic continuity relative to the laurite host ([Fig. 5-B2-B3](#); [Appendix 5](#))
407 point to the existence of droplets of Fe-oxide melt(s) during crystallization of laurite.
408 It is well known that at oxygen fugacity close to the FMQ buffer and ~1000°C, partial
409 melting may produce desulfurization of MSS ([Jugo et al., 2010](#)). This drop in fS_2 is
410 usually exacerbated as S becomes exhausted in the sulfide, because the metal/S ratios
411 of residual sulfide reach the metal eutectic. The result of these processes could not
412 only be the partial desulfurization of the pre-existing MSS but also its subsequent
413 breakdown (either solid or liquid) and the possible formation of oxysulfide melt.
414 Available experiments for the Fe-O-S system at 900-1200 °C indicate that sulfide-
415 oxide melts are stable over a large temperature interval and at oxygen fugacity
416 ranging from the stability field of iron to levels close and above the QFM buffer at
417 any given pressure. In these experiments, magnetite is frequently included in
418 immiscible sulfide blebs formed at high temperatures from common basaltic melts
419 ([Naldrett, 1969](#); [Doyle and Naldrett, 1987](#); [Shishin et al., 2015](#)). For instance,
420 analogous micro-textures to observed here with rounded magnetite inclusions within

421 droplets of BMS have been already reported in peridotite xenoliths from the SCLM
422 (e.g., [Bishop et al., 1975](#); [Guo et al., 1999](#)), sub-arc xenoliths (e.g., [Melekhova et al.,](#)
423 [2017](#)) and modern basaltic lavas (e.g., [Larocque et al., 2000](#); [Zelenski et al., 2017a](#)).
424 These microtextures were ascribed to sulfide-oxide immiscibility at high
425 temperatures. In the scenario proposed above for partial melting of MSS, small
426 fluctuation of fO_2 may have induced sulfide-oxide melt immiscibility giving rise to
427 laurite that mechanically trapped smaller volumes of immiscible Fe-oxide melt
428 concomitant with the crystallization of “residual” MSS. Nevertheless, the mechanism
429 we propose needs of additional experiments determine precisely the phase
430 relationships in the O-S-Fe-Ni system also involving Ru, Os and Ir.

431 To summarize, the composite sulfide assemblage enclosed in the olivine grain
432 from Tres Lagos consisting of Ni-rich pyrrhotite + pentlandite + laurite + Pt-Fe alloy
433 is likely to have formed as a consequence of S removal from a precursor MSS during
434 partial melting and oxidation at high temperatures. In detail, such a mechanism would
435 imply the magmatic precipitation of laurite and Pt-Fe alloys directly from the melt,
436 rather than an origin by exsolution from solid MSS as it was commonly suggested in
437 the literature. This mechanism can apply to other laurite and Os-Ir±Pt-Fe alloy
438 assemblages reported in mantle peridotites associated with residual MSS enclosed in
439 olivine, such as those from the Udachnaya kimberlite in the Siberian Craton ([Griffin](#)
440 [et al., 2002](#)) and the Lherz Massif ([Luguet et al., 2007](#)). Nevertheless, additional TEM
441 analyses are necessary to confirm this hypothesis. [Luguet et al., \(2007\)](#) noted that this
442 type of PGM-BMS assemblage were only present in the most S-poor harzburgite
443 sample from the Lherz massif, which experienced 19-25% of melt extraction.
444 Interestingly, the strongly depleted peridotite from Tres Lagos (sample TL2-1)
445 experienced a minimum of 14-18% partial melting ([Tassara et al., 2018](#)).

446 *4.2. Nano-PGM in BMS hosted within metasomatic pyroxene and carbonate-* 447 *phosphate*

448 The PGM-bearing BMS within metasomatic pyroxenes from Patagonian and
449 Tallante xenoliths studied here also exhibit droplet-like morphology ([Figs. 6A-E](#) and
450 [Appendix 6](#)), suggesting their mechanical entrapment in molten state. Sulfide droplets
451 likely represent immiscible PGE-bearing sulfide melt(s) that were segregated from the

452 metasomatic silicate melt that precipitated the pyroxene (Andersen et al., 1987;
453 Bockrath et al., 2004a; Gaetani and Grove, 1999; Robertson et al., 2016).

454 Platinum is exclusively found at the margin of chalcopyrite forming a
455 composite grain with pentlandite and Ni-rich pyrrhotite in Tres Lagos xenolith (Fig.
456 6A). The reconstructed composition of the sulfide droplet hosting native Pt falls
457 within the compositional mixing line between Ni-rich pyrrhotite and pentlandite
458 (Appendix 4), suggesting that this assemblage resulted from the subsolidus re-
459 equilibrium of MSS and the solid products of a coexisting Ni- and Cu-rich sulfide
460 melt. The irregular contacts between pyrrhotite and pentlandite (Fig. 6A) indicate that
461 the Ni excess in the Fe-sulfide formed flame-like pentlandite exsolution. Canonical
462 views hold that Pt-rich PGM at the margins of mantle BMS originated after sub-
463 solidus transformations of BMS, owing the little ability of MSS and Intermediate
464 Solid Solution (ISS) to incorporate Pt in their structures (Fleet et al., 1993; Li et al.,
465 1996; Peregoedova et al., 1998; Mungall et al., 2005; Holwell et al., 2015). However,
466 the exclusive association of native platinum nanoparticles at the bleb margin of the
467 Tres Lagos xenolith may also indicate a precipitation of the PGM earlier than the
468 BMS. In fact, recent experimental data show that Pt may form its own mineral in Fe-
469 Ni-Cu sulfide melts before the formation of MSS and ISS (Peregoedova and
470 Ohnenstetter, 2002; Sinyakova et al., 2016, 2019). The formation of Pt metal or alloy
471 is favored in the sulfide melt if it was somehow stripped of, or lack semimetals
472 (Helmy et al., 2019).

473 The Pt-Te-Sn compounds were found within isolated pentlandite grains from
474 the Tallante xenoliths (Fig. 6C-D) or at the mutual contacts between pentlandite and
475 chalcopyrite in composite grains from both Tallante and Cerro Redondo xenoliths
476 (Fig. 6B and E). Pentlandite ± chalcopyrite aggregates in metasomatic pyroxenes have
477 been usually interpreted as the product of precipitation of a metasomatic (mobile) Cu-
478 (Ni-Fe)-rich melt formed after incongruent partial melting of a precursor MSS
479 (Luguet and Reisberg, 2016). The first solid product of crystallization of these types
480 of metasomatic Ni- and Cu-rich sulfide melts is the quaternary solid solution
481 consisting of Heazlewoodite [(Ni,Fe)_{3±x}S₂] solid solution (Hz_{ss}) and ISS
482 [(Cu_{1±x},Fe_{1±y})S₂] (ISS) at 900-850°C. These could subsequently exsolve pentlandite
483 from Hz_{ss} at temperature ~760 °C and chalcopyrite from ISS below 557 °C (Kullerud

484 [et al., 1969](#); [Fleet and Pan, 1994](#); [Peregoedova and Ohnenstetter, 2002](#)). The presence
485 of isolated grains of pentlandite and their sharp contacts with chalcopyrite in the
486 inclusions shown in [Figs. 6B-C](#) is consistent with such a fractional crystallization
487 sequence.

488 Tatyanaite grains (ideally $\text{Pt}_9\text{Cu}_3\text{Sn}_4$) found in Tallante xenoliths exhibit well-
489 developed crystal faces and straight contacts with pentlandite and chalcopyrite,
490 although exhibiting a different orientation of the crystal lattice ([Figs. 6E-1, 7, 8](#) and
491 [9](#)). These observations, together with the uniform distribution of Pt-Te-Sn among both
492 chalcopyrite and pentlandite, suggest that these minerals crystallized from melt before
493 the solidification of the high-temperature precursors of these two BMS. This
494 hypothesis is consistent with the high solidus temperatures of these types of PGM
495 ($>1200\text{-}1400\text{ }^\circ\text{C}$; [Shelton et al., 1981](#); [Kravchenko, 2009](#)) and the experimental results
496 of [Sinkyakova et al. \(2016, 2019\)](#), where a wide suite of nano- to micron-sized Pt-Te-
497 Sn minerals crystallized before BMS in a fractionating Cu-rich sulfide melt. This
498 interpretation agrees with the high-temperature origin of pentlandite-hosted
499 moncheite (PtTe_2) in pyroxenites of the Ronda ultramafic massif ([Gutiérrez-Narbona](#)
500 [et al., 1999](#)). However, this hypothesis contrasts with the origin of a Pd-Sn compound
501 (very likely paalovite, Pd_2Sn) hosted in metasomatic clinopyroxene from Mount
502 Porndon by low-temperature exsolution ([Mitchell et al., 1981](#)).

503 Our new interpretation that PGM form by high temperature crystallization
504 prior to their hosting BMS may also apply to the micron-sized cooperite (PtS)
505 intimately associated with chalcopyrite in pyrrhotite-pentlandite-chalcopyrite-
506 carbonate composite blebs reported by [Hughes et al. \(2016\)](#) in xenoliths from the
507 cratonic Hebridean Terrane in Scotland. Those PGM were also attached to BMS
508 suggesting the crystallization of the Pt-sulfide from the Cu-rich sulfide melt before
509 ISS precursor to chalcopyrite. Several experiments in the Pt-Ni-Fe-Cu-S system have
510 shown that cooperite can crystallize directly out from sulfide melts of the three
511 ternary subsystems Fe-Ni-S, Cu-Fe-S and Cu-Ni-S at $>900\text{ }^\circ\text{C}$ ([Makovicky, 2002](#);
512 [Peregoedova and Ohnenstetter, 2002](#); [Sinyakova et al., 2016](#)).

513 [Alard et al. \(2011\)](#) and [Delpech et al. \(2012\)](#) also proposed carbonate and
514 phosphate-rich metasomatism to explain the origin of Pt-Pd-As (including sperrylite,
515 PtAs_2) and Pt-Te-Bi minerals that they identified in composite sulfide blebs of

516 pyrrhotite ± pentlandite ± cubanite ± carbonate ± phosphate found in the Montferrier
517 xenoliths and in dunite xenoliths from Kerguelen. Interestingly, these Pt-Pd-rich Te-
518 Bi-As minerals reported in xenoliths were also found attached to sulfide blebs or at
519 the mutual contact between the BMS. A renewed look of this micro-textural
520 relationship provides an alternative scenario for the formation of all these Pt-Pd-rich
521 Te-Bi-As minerals related after their direct precipitation from sulfide melts at high-
522 temperatures. The nucleation of these types of PGM directly from the sulfide melt is
523 enhanced whenever PGE are dissolved in the liquid as PGE + semimetal complexes
524 (Sinyakova et al., 2016; Helmy et al., 2019). These complexes are formed by the
525 clustering of hundreds of atoms of PGE + semimetal, which could help to overcome
526 the kinetic barrier of nucleation (due to low concentration of PGE in melt) of the
527 nano- and micron-sized PGM, thus acting as seeds for the crystallization of larger
528 microscopic BMS (Helmy et al., 2013; Junge et al., 2015). Alternatively, these Pt-Pd-
529 rich Te-Bi-As minerals could crystallize from nano-to micron-scale droplets of PGE-
530 bearing Te-Bi-As melts immiscible with sulfide droplets they are in contact. This
531 process may take place at >1000 °C, as observed in recent experimental works
532 (Anenburg and Mavrogenes, 2020; Helmy and Botcharnikov, 2020).

533 4.3. Nano-PGM associated with BMS entrained in silicate glasses

534 Platinum nanoparticles are relatively common in pentlandite blebs entrained in
535 silicate glasses from the locality of Gobernador Gregores in southern Patagonia (Fig.
536 10A) and the La Breña in Central Mexico (Fig. 10B-C and 11F-G). The identification
537 of oxy-hydroxides replacing some of the Mexican pentlandite grains suggests that
538 mantle sulfides experienced *in situ* partial desulfurization followed by oxidation,
539 probably under conditions of weathering of the host silicate glass at near-surface
540 temperatures (Szabó and Bodnar, 1995). O'Driscoll and González-Jiménez (2016)
541 interpreted similar Pt-Fe nanoalloys located at edges of partly desulfurized MSS in
542 mantle xenoliths from Calatrava (southwestern Spain) as PGE that, initially dissolved
543 in BMS, were locally remobilized when BMS experienced desulfurization and
544 oxidation.

545 However, many other mantle xenoliths from Gobernador Gregores and Cerro
546 Redondo contain nanoparticles (~20-80 nm) of Pt-rich alloys and arsenides hosted in
547 unaltered BMS (pentlandite, millerite and MSS) entrained within silicate glasses

548 interstitial to the silicate mineral assemblage (González-Jiménez et al., 2019). The
549 investigation of four of these Pt-rich nanoparticles hosted in two pentlandite droplets
550 from Gobernador Gregores (sample GG-14) and Cerro Redondo (sample CR-07) by
551 González-Jiménez et al., (2019) using FIB/HRTEM revealed that these nanoparticles
552 consist of polycrystalline aggregates < 10 nm that are randomly oriented relative to
553 their sulfide host matrices. Since Pt-rich nanoparticles usually consist of aggregates
554 formed by smaller crystals (<10 nm), their formation may be have resulted by
555 clustering of smaller Pt nanoparticles in sulfide melts prior to the crystallization of
556 their hosting BMS (González-Jiménez et al., 2019). This interpretation is consistent
557 with phase relations in the Pt-Fe-Ni-S system predicting the formation of Pt-rich
558 alloys with Fe- and Ni-bearing sulfide melts in equilibrium at >1100-1300 °C (e.g.,
559 Majzlan et al., 2002) and experiments reviewed by Pruseth and Palme (2004) where
560 Pt and Pt-Fe nanoalloys also formed in Fe-rich sulfide melts at fO_2 defined by the
561 QFM buffer.

562 The above discussion points out that, although the formation of Pt
563 nanoparticles in BMS located within interstitial silicate glasses in mantle xenoliths is
564 possible after oxidative weathering of PGE-bearing BMS (e.g., Fig. 10A-D), many of
565 these could also represent primary phases formed from sulfide melts migrating
566 through the SCLM as droplets entrained in silicate (basaltic) melts. As noted above,
567 the precipitation of native Pt or Pt-rich nanoalloys before BMS is promoted whenever
568 ligands such as Te, As, Sb, Bi are not available in the sulfide melt (e.g., Piña et al.,
569 2012). In contrast, Te and/or As, when available in the melt could form nanograins of
570 Pd-Te (possibly merenskyite, PdTe₂) as those observed in the pentlandite-chalcopyrite
571 grain shown in Fig.10E, and Pt-As (possibly sperrylite PtAs₂) as those at contact
572 between pentlandite and millerite shown in Figs. 10F-G.

573 A sulfide bleb entrained in the interstitial glass of xenoliths from Gobernador
574 Gregores also contains Pd-S compounds (possibly braggite, PdS) located at the
575 contact between pyrrhotite and pentlandite (Fig. 10D and D-1; sample GG-01). This
576 sulfide bleb was originally transported in a silicate melt that crystallized at 1064-998
577 °C (Appendix 1). This pentlandite-pyrrhotite assemblage likely formed after the
578 subsolidus re-equilibration of a precursor MSS that crystallized at high temperatures
579 from a sulfide droplet rich in Ni and Fe and depleted in Cu. Experiments show that Pd
580 is relatively incompatible in MSS relative to Cu-Ni rich sulfide melts

581 ($D_{\text{Pd}}^{\text{mss/sulf}}=0.005-0.44$; Fleet et al., 1993; Li et al., 1996; Mungall et al., 2005; Brennan
582 et al., 2016). Therefore, pentlandite derived by re-equilibration of a MSS is expected
583 to contain very little Pd. However, other experimental work (e.g., Makovicky et al.,
584 1986) has shown that at high temperature (900 °C) MSS can dissolve up to 11 wt.%
585 Pd, but when temperature falls the solubility of Pd decreases dramatically (≤ 0.4 wt.%
586 at 500 °C). The results of these experiments indicate that, upon cooling of MSS, Pd
587 should enter in the structure of pentlandite instead of MSS. This inference is
588 consistent with the fact that Pd-rich pentlandite coexists with Pd-poor pyrrhotite in
589 several Ni-Cu deposits (Barnes and Dare, 2010; Piña et al., 2012) and mantle
590 xenoliths (Luguet and Reisberg, 2016; Tassara et al., 2018). The observation of
591 braggite at the contact between pentlandite and pyrrhotite may suggest that Pd was
592 initially incorporated into MSS and then partitioned into pentlandite at ≤ 610 °C.
593 However, other experiments have shown that solid PdS may crystallize from sulfide
594 melt in equilibrium with MSS below 912°C in the Pd-Fe-S system (Makovicky et al.,
595 1988; Makovicky and Karup-Møller, 1993) and at 900 °C in the Pd-Ni-S systems
596 (Karup-Møller and Makovicky, 1993). Additional studies of the Pd-Fe-Ni-S system
597 (Makovicky et al., 1990; Makovicky and Karup-Møller, 1993) also showed the co-
598 crystallization of PdS and MSS [(Fe,Ni)_{1-x}S] at 900°C, with the association PdS-MSS
599 still stable down to 725 °C but decomposing at lower temperature into PdS ±
600 pentlandite ± pyrrhotite (Makovicky, 2002). On the basis of the aforementioned
601 experimental studies, we suggest that natural PdS, like those identified in the BMS
602 bleb from the Gobernador Gregores xenolith, may have also formed at magmatic
603 temperatures preceding the formation of the enclosing MSS. Nevertheless, additional
604 TEM studies are required to confirm this hypothesis.

605 4.4. Nano-PGM embedded in silicate glasses

606 Mantle xenoliths from Gobernador Gregores and Cerro Redondo contain
607 abundant nano-sized particles of Pt-rich alloys dispersed within interstitial silicate
608 glasses (e.g., Fig. 3a-b in González-Jiménez et al., 2019). Frequently, these Pt-rich
609 alloys are adhering to co-genetic oxides (ilmenite or Cr-Spinel) also embedded within
610 the silicate glass. In fact, experimental studies have shown the crystallization of Pt
611 and Pt-Fe nanoparticles at >1000 °C from basaltic melts buffered with $f\text{O}_2$ near the
612 quartz-fayalite-magnetite (QFM) buffer often in presence of Cr-Fe-Ti oxides (Médard

613 [et al., 2015](#); [Anenburg and Mavrogenes, 2016](#)). The results of the experiments also
614 show that, in alkaline melts at fO_2 near the QFM buffer, the crystallization of oxides
615 (ilmenite or Cr-spinel) from the parental alkaline melt may lower fO_2 enough to
616 promote the precipitation of Pt dissolved in the basaltic melt as Pt-rich nanoparticles
617 (e.g., [Anenburg and Mavrogenes, 2016](#)). Notably, Pt-Fe alloys ($\sim Pt_{0.83}Fe_{0.17}$) have
618 been reported included in Cr-spinel from picritic lavas from the active Ambae
619 volcano, in Vanuatu ([Fig. 1](#); [Kamenetsky et al., 2015](#) and references therein),
620 providing an additional case in nature for the direct precipitation of Pt-rich alloys
621 from silicate magmas.

622 On the other hand, two discrete grains of a Ru-S compound (possibly laurite,
623 RuS_2) were identified as isolated crystals embedded in the interstitial glass of mantle
624 xenoliths from southern Patagonia in Cerro Redondo (replicate sample CR-08) and
625 Pali-Aike (sample PA-LA7) ([Figs. 10H-J](#)). These two laurites could be interpreted in
626 two ways: (1) as xenocrysts physically entrained by metasomatic silicate melt or, (2)
627 minerals crystallized from such melt that now is preserved as a quenched glass. The
628 first hypothesis implies that these PGM were residual grains after the complete
629 consumption of precursor BMS during melting or melt-rock reactions taking place in
630 the mantle peridotite (e.g., [Fonseca et al., 2012](#)). The second possibility is sustained
631 by several experimental and empirical results, showing that laurite may crystallize as
632 the earliest liquidus phase at ~ 1200 - $1300^\circ C$ from sulfide-undersaturated basaltic
633 melts ([Brenan and Andrews, 2001](#); [Andrews and Brenan 2002](#); [Bockrath et al.,](#)
634 [2004b](#)). Experimental work on simple basalt analogues in the system SiO_2 - Al_2O_3 -
635 MgO - CaO - Cr_2O_3 (CrMAS), together with thermodynamic consideration of the
636 relevant equilibria, suggest that there is a “window” in the fS_2 - fO_2 - T space in which
637 laurite may precipitate from silicate melt while immiscible sulfide melts are unstable.
638 The size of this window is a function of fO_2 and to a lesser extent of the FeO content
639 in the silicate melt ([Andrews and Brenan, 2002](#); [Bockrath et al., 2004b](#)). Thus,
640 magmatic laurite can crystallize more easily from oxidized silicate melts with fO_2
641 higher than $\Delta QFM = -1.5$, conditions that apply to the late infiltrating melt (i.e., the
642 glassy veins) that bear the laurites in the Cerro Redondo and Pali-Aike peridotites
643 ([Tassara et al., 2020](#)). However, some experiments have shown that a Ru metal
644 nugget preceded many magmatic laurite grains and then reacted with sulfur once fS_2
645 increased in the silicate melt ([Bockrath et al., 2004b](#)). This mechanism has been

646 related to the crystallization of Fe-Ti-Cr-oxides (ilmenite and Cr-spinel) and/or
647 silicates (e.g., secondary pyroxene or olivine) that promotes local perturbations in fO_2
648 at their melt-solid interfaces necessary for the precipitation of Ru (also Os and Ir) as
649 metallic nanoparticles. As noted above, this is a feasible scenario for the cases of
650 Cerro Redondo and Pali-Aike in southern Patagonia where the interstitial glass
651 contains frequent newly-formed oxides and silicates.

652 *4.5. Transport and precipitation of gold nanoparticles in magmas migrating through* 653 *the SCLM*

654 Gold-bearing millerite/pentlandite \pm chalcopyrite composite grains have been
655 found as metasomatic pyroxenes-hosted inclusions in Tallante xenoliths (southeast
656 Spain) (Fig. 11A-B) and entrained within interstitial glass from Cerro Redondo
657 xenoliths in southern Patagonia (Fig. 11C-D and 12). These composite sulfide grains
658 likely correspond to the solid products of Ni-Cu-(Fe) sulfide melts segregated from,
659 or transported by, the metasomatic silicate melts at upper mantle conditions (Tassara
660 et al., 2018). A similar origin can be assumed for the partly altered pentlandite from
661 La Breña in central Mexico (Fig. 11F-G) and Matsoku in northern Lesoto (Appendix
662 7).

663 Experiments in the Fe-Ni-Cu-S system indicate that gold is incompatible in
664 MSS having strong preference for Cu-rich melts (Li and Audétat, 2013; Mungall et
665 al., 2005). Upon crystallization of Cu-rich melts, gold may reach concentrations up to
666 thousands of ppm in ISS, but it is almost insoluble into low-T phases such as
667 chalcopyrite and pentlandite (Piña et al., 2012; Djon and Barnes 2012). However,
668 some empirical results have shown that gold may not partition in ISS if it becomes
669 sufficiently enriched in the Cu-(Ni-Fe)-rich melts to form its own minerals (e.g.,
670 Barnes et al., 2006; Holwell et al., 2015). In the xenoliths studied here, euhedral Au
671 nanoparticles with crystal habits typical of the cubic system are located in both
672 chalcopyrite and pentlandite (e.g., Fig 11D and 12). This suggests their potential
673 formation before the crystallization of the high-temperature precursors of the hosting
674 BMS. In fact, the recent experiments by Sinyakova et al. (2019) indicate the
675 crystallization of gold at high temperatures (> 1000 °C) from Ni-Cu-Fe sulfide melts
676 before BMS. This interpretation could be consistent not only with the presence of
677 euhedral crystals of gold in millerite (Fig. 12), but also of clusters of native Au

678 nanoparticles in the chalcopyrite portion of pentlandite-chalcopyrite grains from the
679 interstitial glass of Cerro Redondo xenolith (see Fig. 2h in [Tassara et al., 2017](#)).

680 It is important to note that the interstitial silicate glass of Cerro Redondo
681 xenoliths also host several isolated gold particles not directly associated with BMS
682 (see Fig. 2f in [Tassara et al., 2017](#)). Decreasing pressure or increasing fO_2 during the
683 melt-rock reaction associated with silicate melt infiltration would increase the S
684 solubility ([Mavrogenes et al., 1999](#); [Jugo et al., 2010](#)), promoting the partial
685 dissolution of the Ni-Cu sulfide blebs into the silicate melt and the release of the gold
686 particles ([Tassara et al., 2020](#)). If liberated to the surrounding silicate melt, the high
687 Au solubility in the silicate melt would result in the partial resorption of these
688 particles. This scenario explain well why gold is euhedral when included in the
689 sulfides, but it is anhedral when included in the interstitial silicate glass as those
690 observed by [Tassara et al. \(2017\)](#).

691 Alternatively, Au particles found in these BMS and silicate glasses could
692 correspond to xenocrysts or particles precipitated earlier from silicate melt. Gold
693 solubility in silicate melts increases as the content of alkali metals and fS_2 in the
694 system both increase ([Li et al., 2019](#)), and if S is present as both reduced (S^{2-}) and
695 oxidized (S^{6+}) species ([Li and Audéat, 2013](#)). In this scenario, the segregation of
696 immiscible Ni-Cu sulfide melts or the incorporation of sulfur dissolved in the silicate
697 melt into the crystallizing Ni-Cu sulfides would decrease gold solubility, triggering its
698 precipitation.

699 Interestingly, [Zelenski et al. \(2017b\)](#) and [Kamenetsky and Zelenski \(2020\)](#)
700 have reported several particles (<100 nm to 3 μm , with the majority falling in the
701 range of 200–500 nm) made up of, sulfides, and alloys of Pd, Pt, Au, Pb, and Bi
702 within sulfide melt inclusions in primitive olivine phenocrysts from the Tolbachik arc
703 volcano, Kamchatka. These gold and PGM particles were found within sulfide
704 matrices or, more commonly, at the contacts between the different BMS (i.e., MSS-
705 ISS, pentlandite-ISS), suggesting the early-magmatic origin of the PGM and gold
706 particles. Micron-sized particles of native gold have also been documented in the
707 glassy groundmass of lamproite dikes from El Tale in southern Spain ([Toscani, 1994](#))
708 and basanite lavas from Hawaii ([Sisson et al. 2003](#)) ([Fig. 1](#)), suggesting direct
709 crystallization of gold from alkali-rich silicate magmas. Moreover, [Zhang et al.](#)

710 (2006) have also reported a bleb of pure Au (~30 μm in diameter) enclosed in a fresh
711 olivine phenocryst from picrites in southwestern China. This Au bleb was interpreted
712 as a xenocryst from the deep mantle transported to shallow depths by a rising plume
713 and then captured by picritic melts.

714 All the observations described above support the hypothesis of a magmatic
715 origin of gold minerals in the SCLM. These gold particles could be interpreted as
716 primary precipitates from the metasomatic (mobile) Ni-Cu-(Fe) sulfide melt, or even
717 silicate melts. However, it cannot explain the micron-sized grains of native gold
718 found in Lherz peridotites containing PGM (Lorand et al., 2010). According to
719 Lorand et al, (2010), these gold particles were detected inside cracks or altered
720 contact between pentlandite and chalcopyrite. Furthermore, gold nanoparticles
721 (including native gold, novodneprite and anyuinite) identified by Ferraris and Lorand
722 (2015) included in olivine from other Lherz peridotite are better explained by
723 circulation of Au-rich fluids during a secondary olivine grains growth. As noted
724 above, a process of plastic deformation enhanced the formation of edge dislocations
725 within olivine grains and thus, the circulation within them of Au-enriched fluids
726 (Ferraris and Lorand, 2015).

727 **5. Conclusions and broader implications**

728 The observations provided in this paper highlight that HSE are not only
729 incorporated as trace-metals into BMS but also as discrete nano- to-micron sized
730 minerals and particles in rocks of the SCLM. The microstructural position of HSE-
731 bearing minerals within mantle peridotites is an important constraint to define
732 whether they resulted by partial melting or metasomatic processes. Whereas HSE-
733 bearing minerals enclosed in residual olivine, or located along interstices of primary
734 minerals, are regarded to have crystallized as a result of melt extraction events, those
735 associated with metasomatic phases (pyroxenes, carbonate-phosphate and interstitial
736 silicate glasses) are formed after melt percolation and melt-peridotite interactions. The
737 formation and stability of these mineral particles predominantly depends on
738 temperature, $f\text{O}_2$, and the activities of chalcogens such as S, As, Te, and Bi in melts.
739 We show that a whole suite of nano-to-micron-sized discrete minerals of the HSE
740 (alloys, sulfides, arsenides, bismuthides, tellurides) can be stable in both silicate and
741 sulfide melts present in the SCLM. The origin of PGM and gold minerals in these

742 textural positions is often related with their direct crystallization from melts in the
743 mantle rather than exsolution from host minerals, regardless their residual or
744 metasomatic origin. Importantly, we highlight that the mechanism of fractionation
745 and transport of the HSE in mantle melt is not exclusively related to their chemical
746 high sulfide/silicate partition coefficient, because nanoparticles may also exert a key
747 role. The latter may impose a significant fraction of the HSE in silicate and sulfide
748 mantle melts. This conclusion is not only sustained by our observation of HSE-
749 bearing nano-scale minerals in the interstitial glass of many mantle rocks but also by
750 the presence of similar HSE-NPs in erupted lavas and experimental results.

751 Our observations highlight that if a fraction of the HSE is incorporated into the
752 melt as nanoparticles or immiscible nano-melts by physical processes during partial
753 melting of mantle peridotite, they could potentially represent a significant repository
754 for HSE in the silicate melts. Thus, mantle melts *en route* toward the crust may
755 transport these sulfide droplets and their cargo of HSE-nanoparticles (HSE-NPs) or
756 nano-melts (HSE-NMs), exerting a yet unforeseen control on the ore potential of
757 primitive metal-rich magmas as in the following cases:

758 (1) *Magmatic Ni-Cu-(PGE) and PGE (sulfide) deposits*: These types of
759 deposits are genetically linked to mantle melts that accessed the crust through trans-
760 lithospheric discontinuities in tectonically active craton margins. Clusters of HSE-
761 NPs (and other chalcophile and siderophile element) might be efficiently partitioned
762 into solid or liquids from these mantle melts to be later concentrated *in-situ* to form
763 the PGE ores. This efficient transport of the HSE as isolated mineral particles should
764 require a relatively fast ascent, which is favored when interconnected magmatic
765 pathways exist between the SCLM and overlying crust (Holwell et al., 2019). In a
766 later stage, the magmas carrying these sulfide melts hosting HSE-NPs or HSE-NMs
767 may be contaminated with crustal material. Some of these “old” HSE-NPs may be
768 preserved in melts while other may combine with semimetals in the zones with higher
769 crustal assimilation allowing the formation of a new suite of HSE-NPs and PGM at
770 crustal conditions. In fact, Pt-rich nanoparticles with identical composition were
771 reported from the Platreef (Junge et al., 2015) and the underlying SCLM (Bultfontain
772 mantle xenoliths; Wainwright et al., 2016). Besides, Hart and Kinloch (1989) reported
773 erlichmanite (OsS₂) grains with mantle-like Os isotopic composition from the

774 Merensky reef. The formation of these erlichmantite grains has been interpreted to
775 predate the main magmatic event of PGE mineralization in the Bushveld Complex,
776 very likely related time of extraction from the mantle melt that supplied PGE to the
777 Bushveld Complex (e.g., [Yudovskaya et al., 2017](#)). The preservation of similar HSE-
778 minerals and Re-Os isotopic signatures can be only explained if metals were
779 efficiently transferred from the mantle to the crust as HSE-NPs. [Holwell et al. \(2011\)](#)
780 noted that initial magmatic sulfides present within the Platreef magma were already
781 highly enriched in PGE and during cooling and crystallization of the sulfide, the PGE
782 tenor were diluted slightly by the addition of country rock sulfur from contamination
783 processes. These observations indicate HSE-NPs-bearing sulfide droplets could be
784 transferred from the SCLM to the overlying crust. Under this new perspective, high
785 tenors in sulfide and/or chromite-rich horizons could be then attributed to the effects
786 of a “second” PGE enrichment owing the role that sulfide and/or oxide like chromite
787 may have also as physical collectors of these mineral particles in the crustal magmatic
788 chamber (e.g., [Mungall, 2005](#)). The implications of our model extend to the transport
789 and deposition of Ni-, Cu- and PGE sulfides in magmatic ore deposits, where it is
790 clearly not safe to assume that sulfide melt always tends to be dissolved upon the
791 quick ascent of the komatiitic magma. This is clearly a fertile field for further
792 investigation.

793 (2) *Au-rich deposits*: The identification of gold minerals in metasomatic
794 silicate glasses and minerals in xenoliths that have sampled the SCLM underlying
795 auriferous continental crusts in Patagonia, Mexico, Spain, Spitsbergen, and Kaapvaal
796 links the fertility of the magmas to the extraction and transport of gold as
797 nanoparticles. This has been proposed as a key ingredient in the production of
798 parental magmas responsible for the formation magmatic-hydrothermal deposits and
799 districts in auriferous crust from Patagonia, Spitsbergen, and Kaapvaal (e.g., [Tassara](#)
800 [et al., 2017](#); [Saunders et al., 2018](#)). The new observations on the presence of several
801 nano-to-micron size particles of gold in pentlandite blebs hosted in metasomatic
802 pyroxene of Tallante in south Spain are also consistent with previous observations
803 from the lamprophyre dykes of El Tale (Fortuna, Province of Murcia). The latter
804 rocks originated from mantle-derived melts also contain particles of up to 5 μm across
805 of native gold derived from a subduction-metasomatized SCLM ([Toscani, 1999](#)).
806 Both xenoliths and lamprophyre dykes are related to the related magmatism that

807 formed Au-Ag epithermal deposits (Carrillo-Rósua et al., 2002). The existence of
808 nanoparticles of gold in partly altered pentlandite blebs hosted in the interstitial glass
809 from La Breña mantle xenoliths could also be linked with a gold-metasomatized
810 mantle. This mantle also underlies a crust with remarkable areal concentration of
811 silver and gold deposits along the San-Luis-Tepehuanes fault system, such as the Ag-
812 Au epithermal deposits of the Concreto de Comonfort, San Lucas de Ocampo and
813 Avino mining districts (Camprubí, 2009).

814 **Acknowledgements**

815 We thank Laurie Reisberg and an anonymous referee for their reviews of the
816 submitted version of the manuscript. This research was supported by Spanish
817 projects: RTI2018-099157-A-I00, CGL2015-65824-P and CGL2016-81085-R
818 granted by the “Ministerio de Ciencia, Innovación y Universidades” and Ministerio de
819 Economía y Competitividad” (MINECO), respectively. Additional funding was
820 provided by the Ramón y Cajal Fellowship RYC-2015-17596 and Junta de Andalucía
821 project B-RNM-189-UGR18 to JMGJ, and the BES-2017-079949 fellowship to ES.
822 This work was also supported by the Mexican research programs CONACYT-Ciencia
823 Básica (A1-S-14574) and UNAM-PAPIIT grant IA-101419 awarded to VC. Research
824 grants, infrastructures and human resources leading to this research have benefited
825 from funding by the European Social Fund and the European Regional Development
826 Fund. We are grateful to Prof. José Jorge Aranda Gómez who provided the xenolith
827 samples of La Breña (Durango Volcanic Field, Central Mexico). María del Mar Abad,
828 Isabel Sánchez Almazo and Rocío Márquez Crespo (CIC, University of Granada) are
829 acknowledged for her assistance with HRTEM, and HR-SEM and FE-SEM analysis,
830 respectively. We are also indebted to Miguel Ángel Hidalgo Laguna from CIC of
831 University of Granada and Xavier Llovet from the *Centres Científics i Tecnològics of*
832 *the Universitat of Barcelona (CCiTUB)* for their careful help with EMPA.

833

834 **References**

835 Alard, O., Griffin, W.L., Pearson, N.J., O'Reilly, S.Y., 2002. New insights into the Re-Os sys-
836 tematics of sub-continental lithospheric mantle from in situ analysis of sulphides. *Earth*
837 *Planetary Science Letters* 203, 651–663.

838 Alard, O., Lorand, J.P., Reisberg, L., Bodinier, J.L., Dutria, J.M., O'Reilly, S.Y., 2011.
839 Volatile-rich metasomatism in Monteferrier xenoliths (Southern France): consequence
840 for chalcophile and highly siderophile element abundance in an orogenic-type
841 subcontinental mantle segment. *Journal of Petrology* doi:10.1093/petrology/egr038.

842 Andersen, T., Griffin, W.L., O'Reilly, S.Y., 1987. Primary sulphide melt inclusions in
843 mantle-derived megacrysts and pyroxenites. *Lithos* 20, 279-294.

844 Andrews, D.R.A., Brenan, J.M., 2002. The solubility of ruthenium in sulfide liquid:
845 implications for platinum group mineral stability and sulfide melt–silicate melt
846 partitioning. *Chemical Geology* 192, 163–181.

847 Anenburg, M., Mavrogenes, J.A., 2016. Experimental observations on noble metal
848 nanonuggets and Fe-Ti oxides, and the transport of platinum group elements in silicate
849 melts. *Geochim Cosmochim Acta* 192, 258–278.

850 Anenburg, M., Mavrogenes, J.A., 2020. Noble metal nanonugget insolubility in geological
851 sulfide liquids. *Geology* <https://doi.org/10.1130/G47579.1>.

852 Augé, T., Genna, A., Legendre, O., Ivanov, K.S., Volchenko, Y.A., 2005. Primary platinum
853 mineralization in the Nizhny Tagil and Kachkanar ultramafic complexes, Urals, Russia:
854 a genetic model for PGE concentration in chromite-rich zones. *Economic Geology* 100,
855 707-732.

856 Barnes, S.-J., Dare, S. A. S., 2010. Pd diffusion into pentlandite evidence from laser ablation.
857 *Goldschmidt Conference Abstract 2010*. p. A54.

858 Barnes, S.-J., C, R., Zientek, M., 2006. Platinum-group element, Gold, Silver and Base Metal
859 distribution in compositionally zoned sulfide droplets from the Medvezky Creek Mine,
860 Noril'sk, Russia. *Contributions to Mineralogy and Petrology*. 152. 187-200.

861 Barnes, S.J., Pagé, P., Prichard, H.M., Zientek, M.L., Fisher, P.C., 2016. Chalcophile and
862 platinum-group element distribution in the ultramafic series of the Stillwater complex,
863 Mt, USA— implications for processes enriching chromite layers in Os, Ir, Ru, and Rh.
864 *Mineralium Deposita*, 51, 25-47.

865 Bishop, F.C., Smith, J.V., Dawson, J.B., 1975. Pentlandite-magnetite intergrowth in De Beers
866 spinel lherzolite: review of sulfide nodules. *Physics and Chemistry of the Earth* 9, 323-
867 337.

- 868 Bockrath, C., Ballhaus, C., Holzheid, A., 2004a. Fractionation of the platinum-group
869 elements during mantle melting. *Science* 305, 1951-1953.
- 870 Bockrath, C., Ballhaus, C., Holzheid, A., 2004b. Stabilities of laurite RuS₂ and monosulphide
871 liquid solution at magmatic temperature. *Chemical Geology* 208, 265–271.
- 872 Brenan, J.M., Andrews, D., 2001. High-temperature stability of Laurite and Ru–Os–Ir alloy
873 and their role in PGE fractionation in mafic magmas. *The Canadian Mineralogist* 39,
874 341–360.
- 875 Brenan, J., Bennett, N., Zajacz, Z., 2016. Experimental Results on Fractionation of the
876 Highly Siderophile Elements (HSE) at Variable Pressures and Temperatures during
877 Planetary and Magmatic Differentiation. *Reviews in Mineralogy and Geochemistry*.
878 81. 1-87. 10.2138/rmg.2016.81.1.
- 879 Camprubí, A., 2009. Major metallogenic provinces and epochs of Mexico. *SGA News*, 25, 1-
880 20.
- 881 Carrillo-Rósua, F.J., Morales-Ruano, S., Hach-Alí, P., 2002. The three generations of gold in
882 the Palai-Islica epithermal deposit, southeastern Spain. *The Canadian Mineralogist* 40,
883 1465-1481.
- 884 Ciobanu, C.L., Cook, N.J., Utsunomiya, S., Pring, A., Green, L., 2011. Focussed ion beam -
885 transmission electron microscopy applications in ore mineralogy: bridging micron-and
886 nanoscale observations. *Ore Geology Reviews* 42, 6–31.
- 887 Delpech, G., Lorand, J-P., Grégoire, M., Cottin, J.Y., O'Reilly, S., 2012. In-situ geochemistry
888 of sulfides in highly metasomatized mantle xenoliths from Kerguelen, southern Indian
889 Ocean. *Lithos* 154, 296-314.
- 890 Djon, M.L.N., Barnes, S-J., 2012. Changes in sulfides and platinum-group minerals with the
891 degree of alteration in the Roby, Twilight, and High Grade Zones of the Lac des Iles
892 Complex, Ontario, Canada. *Mineralium Deposita* 47, 1–22.
- 893 Doyle, C.D., Naldrett, A.J., 1987. The oxygen content of "sulphide" magma and its effect on
894 the partitioning of nickel between coexisting olivine and molten ores. *Economic*
895 *Geology* 82, 208-211.
- 896 Ferraris, C., Lorand, J.P., 2015. Novodneprite (AuPb₃), anyuiite [Au(Pb, Sb)₂] and gold micro
897 - and nano-inclusions within plastically deformed mantle-derived olivine from the

- 898 Lherz peridotite (Pyrenees, France): a HRTEM–AEM–EELS study. *Physics and*
899 *Chemistry of Minerals* 42, 143-150.
- 900 Fleet, M.E., Pan, Y., 1994. Fractional crystallization of anhydrous sulfide liquid in the system
901 Fe-Ni-Cu-S, with application to magmatic sulfide deposits. *Geochimica et*
902 *Cosmochimica Acta* 58, 3369-3377.
- 903 Fleet, M. E., Stone, W. E., 1991. Partitioning of platinum-group elements in the Fe-Ni-S
904 system and their fractionation in nature. *Geochimica et Cosmochimica Acta* 55, 245-
905 253.
- 906 Fleet, M. E., Chryssoulis, S. L., Stone, W. E., and Weisener, C.G., 1993. Partitioning of
907 platinum-group elements and Au in the Fe-Ni-Cu-S system: experiments on the
908 fractional crystallization of sulfide melt. *Contributions to Mineralogy and Petrology*
909 115, 36-44.
- 910 Fonseca, R.O.C., Laurenz, V., Mallmann, G., Luguet, A., Hoehne, N., Jochum, K.P., 2012.
911 New constrains on the genesis and long-term stability of Os-rich alloys in the Earth's
912 mantle. *Geochimica et Cosmochimica Acta* 87, 227–242.
- 913 Fonseca, R.O.C., Brückel, K., Bragagni, A., Leitzke, F.P., Speelmanns, I.M., Wainwright,
914 A.N., 2017. Fractionation of Rhenium from Osmium during noble metal alloy
915 formation in association with sulfides: Implications for the interpretation of model ages
916 in alloy-bearing magmatic rocks. *Geochimica et Cosmochimica Acta* 216, 184-200.
- 917 Gaetani, G.A., and Grove, T.L. ,1999. Wetting of mantle olivine by sulfide melt: Implications
918 for Re/Os ratios in mantle peridotite and late-stage core formation. *Earth and Planetary*
919 *Science Letters* 169, 147-163.
- 920 Garuti, G., Gorgoni, C., Sighinolfi, G.P., 1984. Sulfide mineralogy and chalcophile and
921 siderophile element in the Ivrea-Verbano mantle peridotites (Western Italian Alps).
922 *Earth and Planetary Science Letters* 70, 69-87.
- 923 González-Jiménez., J.M., Gervilla, F., Proenza, J.A., Kerestedjian, T., Augé, T., Bailly, L..
924 2009. Zoning of laurite (RuS₂)-erlichmanite (OsS₂): implications for the genesis of
925 PGM in ophiolite chromitites. *European Journal of Mineralogy* 21, 419-432.
- 926 González-Jiménez, J.M, Roqué-Rosell, J., Jiménez-Franco, A., Tassara, S., Nieto, F.,
927 Gervilla, F., Baurier, S., Proenza, J.A., Saunders, E., Deditius, A., Schilling, M.,
928 Corgne, A., 2019. Magmatic platinum nanoparticles in metasomatic silicate glasses and

- 929 sulfides from Patagonian mantle xenoliths. *Contributions to Mineralogy and Petrology*
930 174, 47.
- 931 Griffin, W.L., Spetsius, Z.V., Pearson, N.J., O'Reilly, S.Y., 2002. In situ Re-Os analysis of
932 sulfide inclusions in kimberlitic olivine: new constraints on depletion events in the
933 Siberian lithospheric mantle. *Geochemistry Geophysics Geosystems* 11, 1069.
- 934 Griffin, W.L., Graham, S., O'Reilly, S.Y., Pearson, N.J., 2004. Lithosphere evolution beneath
935 the Kaapvaal Craton: Re–Os systematics of sulfides in mantle-derived peridotites.
936 *Chemical Geology* 208, 89–118.
- 937 Griffin, W.L., Begg, G.C., O'Reilly, S.Y., 2013. Continental-root control on the genesis of
938 magmatic ore deposits. *Nature Geoscience* 6, 905–910.
- 939 Gutiérrez-Narbona, R., 1999. Implicaciones metalogénicas (cromo y elementos del grupo del
940 platino) de los magmas/fluidos residuales de un proceso de percolación a gran escala en
941 los macizos ultramáficos de Ronda y Ojén (Béticas, Sur de España). Ph. D. Thesis,
942 University of Granada. Spain.
- 943 Guo, J., Griffin, W.L., O'Reilly, S.Y., 1999. Geochemistry and origin of sulphide minerals in
944 mantle xenoliths: Qiling, southeastern China. *Journal of Petrology* 40, 1125-1149.
- 945 Hanley, J., 2007. The role of Arsenic-rich melts and mineral phases in the development of
946 high grade Pt-Pd mineralization within komatiite-associated magmatic Ni-Cu sulfide
947 horizons at Dundonald Beach South, Abitibi Subprovince, Ontario, Canada. *Economic*
948 *Geology* 102, 305–317.
- 949 Hart, S.R., Kinloch, E.D., 1989. Osmium isotope systematics in Witwatersrand and Bushveld
950 ore deposits. *Economic Geology* 84, 1651-1655. DOI: 10.2113/gsecongeo.84.6.1651
- 951 Helmy, H. M., Ballhaus, C., Fonseca, R. O. C., Nagel, T. J., 2013. Fractionation of platinum,
952 palladium, nickel, and copper in sulfide–arsenide systems at magmatic temperature.
953 *Contributions to Mineralogy and Petrology* 166, 1725–1737.
- 954 Helmy, H., Ballhaus, C., Fonseca, R., Leitzke, F., 2019. Arsenic, Te, Se and S Contents in
955 Basaltic Melt at Arsenide, Telluride, Sulfide and Selenide Saturation: the Role of Metal
956 Ligands and Implications for PGM Formation from Silicate Melts. Goldschmidt
957 conference, Barcelona.

- 958 Helmy, H.M., Botcharnikov, R., Experimental determination of the phase relations of Pt and
959 Pd antimonides and bismuthinides in the Fe-Ni-Cu sulfide systems between 1100 and
960 700 °C. *American Mineralogist* 105, 344-352.
- 961 Holwell, D.A., McDonald, I., Butler, I.B., 2011. Precious metal enrichment in the Platreef,
962 Bushveld Complex, South Africa: evidence from homogenised magmatic sulfide melt
963 inclusions. *Contributions to Mineralogy and Petrology* 161, 1011–1026.
- 964 Holwell, D.A., Keays, R.R., McDonald, I., Williams, M.R., 2015. Extreme enrichment of Se,
965 Te, PGE and Au in Cu sulfide microdroplets: evidence from LA-ICP-MS analysis of
966 sulphides in the Skaergaard Intrusion, east Greenland. *Contributions to Mineralogy and
967 Petrology* 170, 53.
- 968 Holwell, D.A., Fiorentini, M., McDonald, I., Lu, Y., Giuliani, A., Smith, D.J., Keith M.,
969 Locmelis, M., 2019. A metasomatized lithospheric mantle control on the metallogenic
970 signature of post-subduction magmatism. *Nature Communications* 10: 3511.
- 971 Hughes, H.S.R. McDonald, I., Faithfull, J.W., Upton, B.G.J., Loocke, M., 2016. Cobalt and
972 precious metals in sulphides of peridotite xenoliths and inferences concerning their
973 distribution according to geodynamic environment: A case study from the Scottish
974 lithospheric mantle. *Lithos* 240-243, 202-227.
- 975 Jugo, P.J., Wilke, M., Botcharnikov, R.E., 2010. Sulfur K-edge XANES analysis of natural
976 and synthetic basaltic glasses: implications for S speciation and S content as function of
977 oxygen fugacity. *Geochimica et Cosmochimica Acta* 74, 5926–5938.
- 978 Junge, M., Wirth, R., Oberthür, T., Melcher, F., Schreiber, A., 2015. Mineralogical sitting of
979 platinum-group elements in pentlandite from the Bushveld Complex, South Africa.
980 *Mineralium Deposita* 50, 41–54.
- 981 Kamenetsky, V.S., Park, J-W., Mungall. J.E., Pushkarev. E.V., Ivanov. A.V., Kamenetsky,
982 M.B., Yaxley, G.M., 2015. Crystallization of platinum-group minerals from silicate
983 melts: Evidence from Cr-spinel–hosted inclusions in volcanic rocks. *Geology* 43, 903–
984 906.
- 985 Kamenetsky, V., Zelenski, M., 2020. Origin of noble-metal nuggets in sulfide-saturated arc
986 magmas: A case study of olivine-hosted sulfide melt inclusions from the Tolbachik
987 volcano (Kamchatka, Russia).

- 988 Karup-Møller, S., Makovicky, E., 1993. The system Pd-Ni-S at 900°, 725°, 550° and 400°.
989 Economic Geology 88, 1261-8.
- 990 Keays, R.R., Sewell, D.K.B., Mitchell, R.H., 1981. Platinum and palladium minerals in upper
991 mantle-derived lherzolites. Nature 294, 646-648.
- 992 Kitakaze, A., Machida, T., Komatsu, R., 2016. Phase relations in the Fe-Ni-S system from
993 875 to 650 °C. The Canadian Mineralogist 54, 1175–1186.
- 994 Kogiso, T., Suzuki, K., Suzuki, T., Shinotsuka, K., Uesugi, K., Takeuchi, A., Suzki, Y.,
995 2008. Detecting micrometer-scale platinum-group minerals in mantle peridotite with
996 microbeam synchrotron radiation X-ray fluorescence analysis. Geochemsitry
997 Geophysics Geosystems 9, Q03018, doi:10.1029/2007GC001888
- 998 König, S., Lissner, M., Lorand, J-P., Bragagni, A., Luguët, A., 2015. Mineralogical control of
999 selenium, tellurium and highly siderophile elements in the Earth's mantle: Evidence
1000 from mineral separates of ultra-depleted mantle residues. Chemical Geology 396, 16–
1001 24.
- 1002 Kravchenko, T.A., 2009. Pt-Pd-Sn intermetallic compounds crystallized from Cu-Fe sulfide
1003 melt. New data on Minerals 44, 66-72.
- 1004 Kullerud, G., Yund, R. A., Moh, G. H., 1969. Phase relations in the Cu-Fe-S, Cu-Ni-S and
1005 Fe-Ni-S systems. In Wilson, H. D. B. ed., Magmatic Ore Deposits, Economic Geology
1006 Publishing Co., Lancaster, Pennsylvania, p.323-343.
- 1007 Larocque, A., Stimac, J., Keith, J., Huminicki, M., 2000. Evidence for open-system behavior
1008 in immiscible Fe-S-O liquids in silicate magmas: implications for contributions of
1009 metals and sulfur to ore-forming fluids. The Canadian Mineralogist 38, 1233-1249.
- 1010 Lee, M., 2010. Transmission electron microscopy (TEM) of earth and planetary materials: a
1011 review. Mineral. Mag. 74, 1–27.
- 1012 Li, Y., Audétat, A., 2013. Gold solubility and partitioning between sulfide liquid,
1013 monosulfide solid solution and hydrous mantle melts: implications for the formation of
1014 Au-rich magmas and crust-mantle differentiation. Geochimica et Cosmochimica Acta
1015 118, 247-262.
- 1016 Li, C., Barnes, S-J., Makovicky, E., Rose-Hansen, J., Makovicky, M., 1996. Partitioning of
1017 nickel, copper, iridium, rhodium platinum and palladium between monosulphide solid

- 1018 solution and sulphide liquid: effects of composition and temperature. *Geochimica et*
1019 *Cosmochimica Acta* 60, 1231-1238.
- 1020 Li, Y., Feng, L., Kiseeva, E.S., Gao, Z., Guo, H., Du., Z., Wang, F., Shi, L., 2019. An
1021 essential role for sulfur in sulfide-silicate melt partitioning of gold and magmatic gold
1022 transport at subduction settings. *Earth And Planetary Science Letters* 528, 115850.
- 1023 Lorand, J.P., Alard, O., Luguet, A., 2010. Platinum-group element micronuggets and
1024 refertilization process in Lherz orogenic peridotite (northeastern Pyrenees, France).
1025 *Earth and Planetary Science Letters* 289, 298–310.
- 1026 Luguet, A., Reisberg, L., 2016. Highly Siderophile Element and ¹⁸⁷Os Signatures in Non-
1027 cratonic Basalt-hosted Peridotite Xenoliths: Unravelling the Origin and Evolution of
1028 the Post-Archean Lithospheric Mantle. *Reviews in Mineralogy and Geochemistry* 81,
1029 305-367.
- 1030 Luguet, A., Shirey, S.B., Lorand, J.P., Horan, M.F., Carlson, R.W., 2007. Residual platinum-
1031 group minerals from highly depleted harzburgites of the Lherz massif (France) and
1032 their role in HSE fractionation of the mantle. *Geochimica et Cosmochimica Acta* 71,
1033 3082–3097.
- 1034 Mann, U., Frost, D., Rubie, D., Becker, H., Audetat, A., 2012. Partitioning of Ru, Rh, Pd, Re,
1035 Ir and Pt between liquid metal and silicate at high pressures and high temperatures -
1036 Implications for the origin of highly siderophile element concentrations in the Earth's
1037 mantle. *Geochimica et Cosmochimica Acta*. 84. 593–613. 10.1016/j.gca.2012.01.026.
- 1038 Makovicky, E., 2002. Ternary and quaternary phase systems with PGE. In: Cabri LJ (ed) *The*
1039 *Geology, Geochemistry, Mineralogy and Mineral Beneficiation of Platinum-Group*
1040 *Elements*. Canadian Institution of Mining Metallurgy and Petroleum, Montreal, pp
1041 131–178.
- 1042 Makovicky, E., Karup-Møller, S., 1993. The system Pd-Fe-S at 900°, 725°, 550° and 400°.
1043 *Economic Geologist* 88, 1269-78.
- 1044 Makovicky, M., Makovicky, E., Rose-Hansen, J., 1986. Experimental studies on the
1045 solubility and distribution of platinum group elements in base metal sulphides in
1046 platinum deposits. In: Gallagher M J, Ixer RA, Neary CR, Priedhard HM (eds)
1047 *Metallurgy of basic and ultrabasic rocks*. The Institution of Mining and Metallurgy,
1048 London, pp 415-425.

- 1049 Makovicky, M., Makovicky, E. and Rose-Hansen, J., 1988. Experimental evidence of the
1050 formation and mineralogy of platinum and palladium ore deposits. In *Mineral Deposits*
1051 within the European Community (J. Boissonnas and P. Omenetto, eds.) Berlin-
1052 Heidelberg, Springer-Verlag, 303-17.
- 1053 Makovicky, E., Karup-Mcfler S., Makovicky, M. and Rose-Hansen, J., 1990. Experimental
1054 studies on the phase systems Fe-Ni-Pd-S and Fe-Pt-Pd-As-S applied to PGE deposits.
1055 *Mineralogy and Petrology*, 42, 307-13.
- 1056 Mavrogenes, J.A., O'Neill, H.S.C., 1999. The relative effects of pressure, temperature and
1057 oxygen fugacity on the solubility of sulfide in mafic magmas. *Geochemica et*
1058 *Cosmochimica Acta* 63, 1173–1180.
- 1059 Majzlan, J., Makovicky, M., Makovicky, E., Rose-Hansen, J., 2002. The system Fe–Pt–S at
1060 1100°C. *The Canadian Mineralogist* 40, 509-517.
- 1061 Médard, E., Schmidt, M.W., Wälle, M., Keller, N.S., Günther, D., 2015. Platinum partitioning
1062 between metal and silicate melts: Core formation, late veneer and the nanonuggets
1063 issue. *Geochimica et Cosmochimica Acta* 162, 183-201.
- 1064 Melekhova, E., Blundy, J., Martin, R., Arculus, R., Pichavant, M., 2017. Petrological and
1065 experimental evidence for differentiation of water-rich magmas beneath St. Kitts,
1066 Lesser Antilles. *Contributions to Mineral and Petrology* 172, 98.
1067 <https://doi.org/10.1007/s00410-017-1416-3>.
- 1068 Mundl, A., Ntaflos, T., Ackerman, L., Bizimis, M., Bjerg, E.A., Wegner, W., Hauzenberger,
1069 C.A., 2015. Geochemical and Os-Hf-Nd-Sr isotopic characterization of North
1070 Patagonian Mantle xenolith: implications for extensive melt extraction and percolation
- 1071 Mungall, J.E., Andrews, D.R.A., Cabri, L.J., Sylvester, P.J., Tubrett, M., 2005. Partitioning of
1072 Cu, Ni, Au, and platinum-group elements between monosulfide solid solution and
1073 sulfide emelt under controlled oxygen and sulfur fugacities. *Geochimica et*
1074 *Cosmochimica Acta* 69, 4349-4360.
- 1075 Mungall, J.E., Brenan, J.M., 2014. Partitioning of platinum-group elements and Au between
1076 sulfide liquid and basalt and the origins of mantle-crust fractionation of the chalcophile
1077 elements. *Geochimica et Cosmochimica Acta* 125, 265-289.
- 1078 Naldrett, A.J., 1969. A portion of the system Fe—S—O between 900 and 1080°C and its
1079 application to sulfide ore magmas. *Journal of Petrology* 10, 171—201.

- 1080 O'Driscoll, B., González-Jiménez, J.M., 2016. Petrogenesis of the Platinum-Group Minerals.
1081 *Reviews in Mineralogy and Geochemistry* 81, 489-578.
- 1082 Peregoedova, A.V., 1998. The experimental study of the Pt-Pd-partitioning behaviour between
1083 monosulfide solid solution and Cu-Ni-sulfide melt at 900-840 °C 8th International
1084 Platinum Symposium Abstracts: Geological Society South Africa and South African
1085 Institute of Mining and Metallurgy Symposium Series S18, pp, 325-327.
- 1086 Peregoedova, A.V., Ohnenstetter, M., 2002. Collectors of Pt, Pd and Rh in a S-poor Fe-Ni-
1087 Cu-sulfide system at 760 °C: experimental data and application to ore deposits. *The*
1088 *Canadian Mineralogist* 40, 527 – 561.
- 1089 Peregoedova, A., Barnes, S.J., Baker, D.R., 2004. The formation of Pt-Ir alloys and Cu-Pd-
1090 rich sulfide melts by partial desulfurization of Fe-Ni-Cu sulfides: results of
1091 experiments and implications for natural systems. *Chemical Geology* 208, 247–264.
- 1092 Piña, R., Gervilla, F., Barnes, S.J., Ortega, L., Lunar, R., 2012. Distribution of platinum-
1093 group and chalcophile elements in the Aguablanca Ni-Cu sulfide deposit (SW Spain):
1094 evidence from a la-ICP-MS study. *Chemical Geology* 302–303, 61–75.
- 1095 Pruseth, K.L., Palme, H., 2004. The solubility of Pt in liquid Fe-sulfides. *Chemical Geology*
1096 208, 223-245.
- 1097 Robertson, J.C., Barnes, S.J., Le Vaillant, M., 2016. Dynamics of magmatic sulphide droplets
1098 during transport in silicate melts and implications for magmatic sulphide ore formation.
1099 *Journal of Petrology* 56, 2445-2472.
- 1100 Saunders, J.E., Pearson, N.J., O'Reilly, S.Y., Griffin, W.L., 2015. Sulphide metasomatism
1101 and the mobility of gold in the lithospheric mantle. *Chemical Geology* 410, 149-161.
- 1102 Saunders, J. E., Pearson, N. J., O'Reilly, S. Y., Griffin, W. L., 2018. Gold in the mantle: a
1103 global assessment of abundance and redistribution processes. *Lithos* 322, 376-391.
- 1104 Shelton, K.L., Merewether, P.A., Skinner, B.J., 1981. Phases and phase relations in the
1105 system Pd-Pt-Sn. *The Canadian Mineralogist* 19, 599-605.
- 1106 Shinshin, D., Jak, E., Deckerov, S.A., Critical assessment and thermodynamic modeling of the
1107 Fe-O-S system. *Journal of Phase Equilibria and Diffusion* 36, 224-240.

- 1108 Sinyakova, E., Kosyakov, V., Distler, V., Karmanov, N., 2016. Behaviour of Pt, Pd, and Au
1109 during crystallization of Cu-rich magmatic sulfide minerals. *The Canadian*
1110 *Mineralogist* 45, 491-509.
- 1111 Sinyakova, E., Kosyakov, V., Palyanova, G., Karmanov, N., 2019. Experimental modeling of
1112 noble and chalcophile element fractionation during solidification of Cu-Fe-Ni-S melt.
1113 *Minerals* 9, 531; doi:10.3390/min9090531.
- 1114 Sisson, T.W., 2003. Native gold in Hawaiian alkali magma. *Economic Geology* 98, 643-648.
- 1115 Sugaki, A., Kitakaze, A., 1998. High form of pentlandite and its thermal stability. *American*
1116 *Mineralogist* 83, 133-140.
- 1117 Szabó, Cs., Bodnar, R.J., 1995. Chemistry and origin of mantle sulfides in spinel peridotite
1118 xenoliths from alkaline basaltic lavas, Nógrád-Gömör Volcanic Field, northern Hungary
1119 and southern Slovakia. *Geochimica et Cosmochimica Acta* 59, 3917-3927.
- 1120 Tassara, S., González-Jiménez, J.M., Reich, M., Schilling, M.E., Morata, D., Begg, G.,
1121 Saunders, E., Griffin, W.L., O'Reilly, S.Y., Grégoire, M., Barra, F., Corgne, A., 2017.
1122 Plume-subduction interaction forms large auriferous provinces. *Nature*
1123 *Communications* 8, 843.
- 1124 Tassara, S., González-Jiménez, J.M., Reich, M., Saunders, E., Luet, A., Morata, D.,
1125 Grégoire, M., van Aken, D., Schilling, M.E., Barra, F., Nowell, G., Corgne, A., 2018.
1126 Highly siderophile elements mobility in the subcontinental lithospheric mantle beneath
1127 southern Patagonia. *Lithos* 314–315, 579–596.
- 1128 Tassara, S., Reich, M., Konecke, B.A., González-Jiménez, J.M., Simon, A.c., Morata, D.,
1129 Barra, F., Fiege, A., Schilling, M.E., Corgne, A., 2020. Unraveling the effects of melt-
1130 mantle interactions on the gold fertility of magmas. *Frontiers in Earth Science* 11.
1131 <https://doi.org/10.3389/feart.2020.00029>.
- 1132 Toscani, L., 1999. Magmatic gold grains in the El Tale lamproite, Fortuna, SE Spain.
1133 *Mineralogical Magazine*, 63, 595-602.
- 1134 Tredoux, M., Lindsay, N.M., Davies, G., McDonald, L., 1995. The fractionation of platinum-
1135 group elements in magmatic systems, with the suggestion of a novel causal mechanism.
1136 *South African Journal of Geology* 98, 157–167.

- 1137 Wainwright, A.N., Luguet, A., Schreiber, A., Fonseca, R.O.C., Nowell, G.M., Lorand J-P,
1138 Wirth, R., Janney, P.E., 2016. Nanoscale variations in ¹⁸⁷Os isotopic composition and
1139 HSE systematics in a Bultfontein peridotite. *Earth and Planetary Science Letters* 447,
1140 60-71.
- 1141 Wang, K.L., O'Reilly, S.Y., Griffin, W.L., Pearson, N.J., Zhang, M., 2009. Sulfides in mantle
1142 peridotites from Penghu Island, Taiwan: melt percolation, PGE fractionation, and the
1143 lithospheric evolution of the South China block. *Geochim Cosmochim Acta* 73, 4531–
1144 4557.
- 1145 Wirth, R., 2004. Focused Ion Beam (FIB): a novel technology for advanced application of
1146 micro- and nanoanalysis in geosciences and applied mineralogy. *Eur. J. Mineral.* 16,
1147 863–876.
- 1148 Wirth, R., 2009. Focused Ion Beam (FIB) combined with SEM and TEM: advanced analyt-
1149 ical tools for studies of chemical composition, microstructure and crystal structure in
1150 geomaterials on a nanometre scale. *Chem. Geol.* 261, 217–229.
- 1151 Wirth, R., Reid, D., Schreiber, A., 2013. Nanometer-sized platinum-group minerals (PGM) in
1152 base metal sulfides: new evidence for an orthomagmatic origin of the Merensky reef
1153 PGE ore deposit. Bushveld Complex. South Africa. *Can. Mineral.* 51, 143–155.
- 1154 Yudovskaya, M., Belousova, E., Kinnaird, J., Dubinina, E., Grobler, D.F., Pearson, N., 2017.
1155 Re-Os and S isotope evidence for the origin of Platreef mineralization (Bushveld
1156 Complex). *Geochimica et Cosmochimica Acta* 214, 282-307.
- 1157 Zelenski, M., Kamenetsky, V.S., Mavrogenes, J.A., Gurenko, A.A., Danyushevsky, L.V.,
1158 2017a. Silicate-sulfide liquid immiscibility in modern arc basalt (Tolbachik volcano,
1159 Kamchatka): Part I. Occurrence and compositions of sulfide melts. *Chemical Geology*
1160 478, 102-111. <http://dx.doi.org/10.1016/j.chemgeo.2017.09.013>
- 1161 Zelenski, M., Kamenetsky, V.S., Navrogenes, J.A., Danyushevsky, L.V., Matveev, D.,
1162 Gurenko, A.A., 2017b. Platinum-group elements and gold in sulfide melts from
1163 modern arc basalt (Tolbachik volcano, Kamchatka). *Lithos* 290-291, 172-188.
- 1164 Zhang, Z., Mao, J., Wang, F., Pirajno, F., 2006. Native gold and native copper grains
1165 enclosed by olivine phenocrysts in a picrite lava of the Emeishan large igneous
1166 province, SW China. *American Mineralogist* 91, 1178-1183.

1167 **Figure captions**

1168 **Figure 1.** Global map showing the distribution of localities sampling rocks of the
1169 Subcontinental Lithospheric Mantle (SCLM) where discrete minerals of the
1170 highly siderophile elements have been reported. This map also includes the new
1171 discoveries of HSE minerals reported in this study. Reference for the different
1172 localities are in the main text.

1173 **Figure 2.** (A) Backscattered images of the PGM-bearing base-metal sulfide bleb
1174 hosted in a residual olivine grain from a peridotite xenolith from Tres Lagos in
1175 southern Patagonia (sample TL-2-1). (B-G) Quantitative, wavelength-
1176 dispersive spectrometry (WDS) X-ray elemental maps of sulfide bleb. Note the
1177 heterogeneous distribution of Ru and Pt indicating the presence of
1178 nanoparticles.

1179 **Figure 3.** Back-scattered images of thin-foil sampled from the Tres Lagos PGM-
1180 bearing base-metal sulfide blebs shown in [Figure 2](#). The three nano-PGM
1181 identified as laurite that were intersected during sample preparation are enclosed
1182 in the rectangles and named as shown in [Figures 4](#) and [5](#).

1183 **Figure 4.** HAADF-STEM images and associated EDS elemental maps for laurites
1184 included in the Tres Lagos PGM-bearing base-metal sulfide bleb shown in
1185 [Figures 2](#) and [3](#). Each laurite nanoparticle is named A, B and C as in [Figures 3](#)
1186 and [5](#). Note the Os-rich rim in laurites (A) and (B), the euhedral shape of laurite,
1187 and the inclusions of magnetite in laurite.

1188 **Figure 5.** HRTEM images of the three nano-PGM included in the Tres Lagos PGM-
1189 bearing base-metal sulfide blebs shown in [Figures 2, 3](#) and [4](#). (A) Low-
1190 magnification and (A1) HR-images of the grain boundary between laurite and
1191 pyrrhotite. Note the polycrystalline nature of pyrrhotite near the grain boundary.
1192 (B, B2) Low-magnification and (B1,3) HR-images of single-crystal of
1193 pentlandite (B1) and spherical inclusions of magnetite in single crystal of laurite
1194 (B3). (C) Low-magnification and (C1) HR-images of grain boundary between
1195 single crystal of pyrrhotite and laurite. Images A1, B1, B3 and C1 include insets
1196 of the Fast Fourier Transform (FFT) of HR image showing diffraction maxima
1197 and Miller indices for the nanoparticles and host sulfide matrices.

1198 **Figure 6.** Backscattered images of the PGM-bearing base-metal sulfide blebs hosted
1199 in metasomatic pyroxenes from southern Patagonian xenoliths of Tres Lagos
1200 (A, A1 and A2) and Cerro Redondo (B), and from Tallante xenolith from
1201 southern Spain (C to E-1).

1202 **Figure 7.** Back-scattered images of thin-foil sampled from the Tallante PGM-bearing
1203 base-metal sulfide bleb shown in [Figure 6E-1](#). The intersected euhedral grain of

1204 nano-PGM is associated with anhedral chalcopyrite at the contact between
1205 pentlandite and clinopyroxene.

1206 **Figure 8.** HAADF-STEM image and EDS elemental mapping of the Pt-Sn
1207 nanoparticle, magnetite, chalcopyrite and hosting pentlandite from Tallante
1208 xenolith shown in [Figure 6E-1](#).

1209 **Figure 9.** Low-magnification and high-magnification HRTEM images and associated
1210 Fast Fourier Transform (FFT) of HR image of the nano-PGM the Tallante
1211 PGM-bearing base-metal sulfide bleb shown in [Figure 6E-1](#) (B) HRTEM image
1212 of the gran boundary between single crystals of pentlandite (see image A) and
1213 tatyanaite (see image C). (D) HRTEM image of grain boundary between
1214 pentlandite and magnetite; note the misorientation and defects between these
1215 two minerals. (E) HR image of single crystal of magnetite.

1216 **Figure 10.** Backscattered electron images of the PGM-bearing base-metal sulfide
1217 blebs hosted in metasomatic interstitial glass in mantle xenoliths (this study).
1218 The suite of nano-PGM include: native Pt in the Patagonian locality of Cerro
1219 Redondo (A to A2) and the Mexican locality of La Breña (B to C-1), PdS
1220 (possibly braggite) and Pt-As (possibly sperrylite) in Cerro Redondo (D-G) as
1221 well as Ru-S (possibly laurite) in Cerro Redondo and Pali-Aike (H-J) also in
1222 Patagonia.

1223 **Figure 11.** Backscattered electron images of the Au-bearing base-metal sulfide blebs
1224 hosted in metasomatic interstitial glass in the mantle xenoliths from Tallante in
1225 southern Spain (A to B1), Cerro Redondo in Patagonia (C to D-1) and La Breña
1226 in central Mexico (E to G-2).

1227 **Figure 12.** (A) Back-scattered electron images of a PGM-bearing base-metal sulfide
1228 bleb identified by [Tassara et al. \(2017\)](#) in a xenolith from the Patagonian
1229 locality of Cerro Redondo ([Figure 2b-c](#) in the cited paper); a thin-foil was
1230 sampled from this sulfide bleb in B. Image C is a HAADF-STEM image of the
1231 thin-foil damaged during thinning. The Au NP was lost. Note the euhedral
1232 shape of the Au NP in image A and B.

1233

1234

1235 **Appendix**

1236 **Appendix 1.** Geological and petrological background information of the samples
1237 employed in this study.

1238 **Appendix 2.** Analytical methods

1239 **Appendix 3.** Chemistry of base-metal sulfides hosting nano- and micron-sized HSE-
1240 minerals from mantle xenoliths analyzed in this study obtained by EPMA.

1241 **Appendix 4.** Back-scattered electron images (BSE), EDS spectra and elemental
1242 mapping of nano-to-microparticles of HSE minerals associated with Ni-Fe-S ternary
1243 diagrams showing the composition of the hosting BMS.

1244 **Appendix 5.** Indexed SAED pattern obtained from minerals shown in Figures 5 and
1245 9.

1246 **Appendix 6.** Time-resolved LA-ICP-MS spectra for nano- and micron-sized minerals
1247 and particles of HSE-minerals identified in this study, and chemical composition of
1248 their host base-metal sulfides in terms of Ni, Fe, and S.

1249

1167 **Figure captions**

1168 **Figure 1.** Global map showing the distribution of localities sampling rocks of the
1169 Subcontinental Lithospheric Mantle (SCLM) where discrete minerals of the
1170 highly siderophile elements have been reported. This map also includes the new
1171 discoveries of HSE minerals reported in this study. Reference for the different
1172 localities are in the main text.

1173 **Figure 2.** (A) Backscattered images of the PGM-bearing base-metal sulfide bleb
1174 hosted in a residual olivine grain from a peridotite xenolith from Tres Lagos in
1175 southern Patagonia (sample TL-2-1). (B-G) Quantitative, wavelength-
1176 dispersive spectrometry (WDS) X-ray elemental maps of sulfide bleb. Note the
1177 heterogeneous distribution of Ru and Pt indicating the presence of
1178 nanoparticles.

1179 **Figure 3.** Back-scattered images of thin-foil sampled from the Tres Lagos PGM-
1180 bearing base-metal sulfide blebs shown in [Figure 2](#). The three nano-PGM
1181 identified as laurite that were intersected during sample preparation are enclosed
1182 in the rectangles and named as shown in [Figures 4](#) and [5](#).

1183 **Figure 4.** HAADF-STEM images and associated EDS elemental maps for laurites
1184 included in the Tres Lagos PGM-bearing base-metal sulfide bleb shown in
1185 [Figures 2](#) and [3](#). Each laurite nanoparticle is named A, B and C as in [Figures 3](#)
1186 and [5](#). Note the Os-rich rim in laurites (A) and (B), the euhedral shape of laurite,
1187 and the inclusions of magnetite in laurite.

1188 **Figure 5.** HRTEM images of the three nano-PGM included in the Tres Lagos PGM-
1189 bearing base-metal sulfide blebs shown in [Figures 2, 3](#) and [4](#). (A) Low-
1190 magnification and (A1) HR-images of the grain boundary between laurite and
1191 pyrrhotite. Note the polycrystalline nature of pyrrhotite near the grain boundary.
1192 (B, B2) Low-magnification and (B1,3) HR-images of single-crystal of
1193 pentlandite (B1) and spherical inclusions of magnetite in single crystal of laurite
1194 (B3). (C) Low-magnification and (C1) HR-images of grain boundary between
1195 single crystal of pyrrhotite and laurite. Images A1, B1, B3 and C1 include insets
1196 of the Fast Fourier Transform (FFT) of HR image showing diffraction maxima
1197 and Miller indices for the nanoparticles and host sulfide matrices.

1198 **Figure 6.** Backscattered images of the PGM-bearing base-metal sulfide blebs hosted
1199 in metasomatic pyroxenes from southern Patagonian xenoliths of Tres Lagos
1200 (A, A1 and A2) and Cerro Redondo (B), and from Tallante xenolith from
1201 southern Spain (C to E-1).

1202 **Figure 7.** Back-scattered images of thin-foil sampled from the Tallante PGM-bearing
1203 base-metal sulfide bleb shown in [Figure 6E-1](#). The intersected euhedral grain of

1204 nano-PGM is associated with anhedral chalcopyrite at the contact between
1205 pentlandite and clinopyroxene.

1206 **Figure 8.** HAADF-STEM image and EDS elemental mapping of the Pt-Sn
1207 nanoparticle, magnetite, chalcopyrite and hosting pentlandite from Tallante
1208 xenolith shown in [Figure 6E-1](#).

1209 **Figure 9.** Low-magnification and high-magnification HRTEM images and associated
1210 Fast Fourier Transform (FFT) of HR image of the nano-PGM the Tallante
1211 PGM-bearing base-metal sulfide bleb shown in [Figure 6E-1](#) (B) HRTEM image
1212 of the gran boundary between single crystals of pentlandite (see image A) and
1213 tatyanaite (see image C). (D) HRTEM image of grain boundary between
1214 pentlandite and magnetite; note the misorientation and defects between these
1215 two minerals. (E) HR image of single crystal of magnetite.

1216 **Figure 10.** Backscattered electron images of the PGM-bearing base-metal sulfide
1217 blebs hosted in metasomatic interstitial [glass in mantle](#) xenoliths (this study).
1218 The suite of nano-PGM include: native Pt in the Patagonian locality of Cerro
1219 Redondo (A to A2) and the Mexican locality of La Breña (B to C-1), PdS
1220 (possibly braggite) and Pt-As (possibly sperrylite) in Cerro Redondo (D-G) as
1221 well as Ru-S (possibly laurite) in Cerro Redondo and Pali-Aike (H-J) also in
1222 Patagonia.

1223 **Figure 11.** Backscattered electron images of the Au-bearing base-metal sulfide blebs
1224 hosted in metasomatic interstitial glass in the mantle xenoliths from Tallante in
1225 southern Spain (A to B1), Cerro Redondo in Patagonia (C to D-1) and La Breña
1226 in central Mexico (E to G-2).

1227 **Figure 12.** (A) Back-scattered electron images of a PGM-bearing base-metal sulfide
1228 bleb identified by [Tassara et al. \(2017\)](#) in a xenolith from the Patagonian
1229 locality of Cerro Redondo ([Figure 2b-c](#) in the cited paper); a thin-foil was
1230 sampled from this sulfide bleb in B. Image C is a HAADF-STEM image of the
1231 thin-foil damaged during thinning. The Au NP was lost. Note the euhedral
1232 shape of the Au NP in image A and B.

1233

1234

1235 **Appendix**

1236 **Appendix 1.** Geological and petrological background information of the samples
1237 employed in this study.

1238 **Appendix 2.** Analytical methods

1239 **Appendix 3.** Chemistry of base-metal sulfides hosting nano- and micron-sized HSE-
1240 minerals from mantle xenoliths analyzed in this study obtained by EPMA.

1241 **Appendix 4.** Back-scattered electron images (BSE), EDS spectra and elemental
1242 mapping of nano-to-microparticles of HSE minerals associated with Ni-Fe-S ternary
1243 diagrams showing the composition of the hosting BMS.

1244 **Appendix 5.** Indexed SAED pattern obtained from minerals shown in Figures 5 and
1245 9.

1246 **Appendix 6.** Time-resolved LA-ICP-MS spectra for nano- and micron-sized minerals
1247 and particles of HSE-minerals identified in this study, and chemical composition of
1248 their host base-metal sulfides in terms of Ni, Fe, and S.

1249

Figure 1
[Click here to download high resolution image](#)

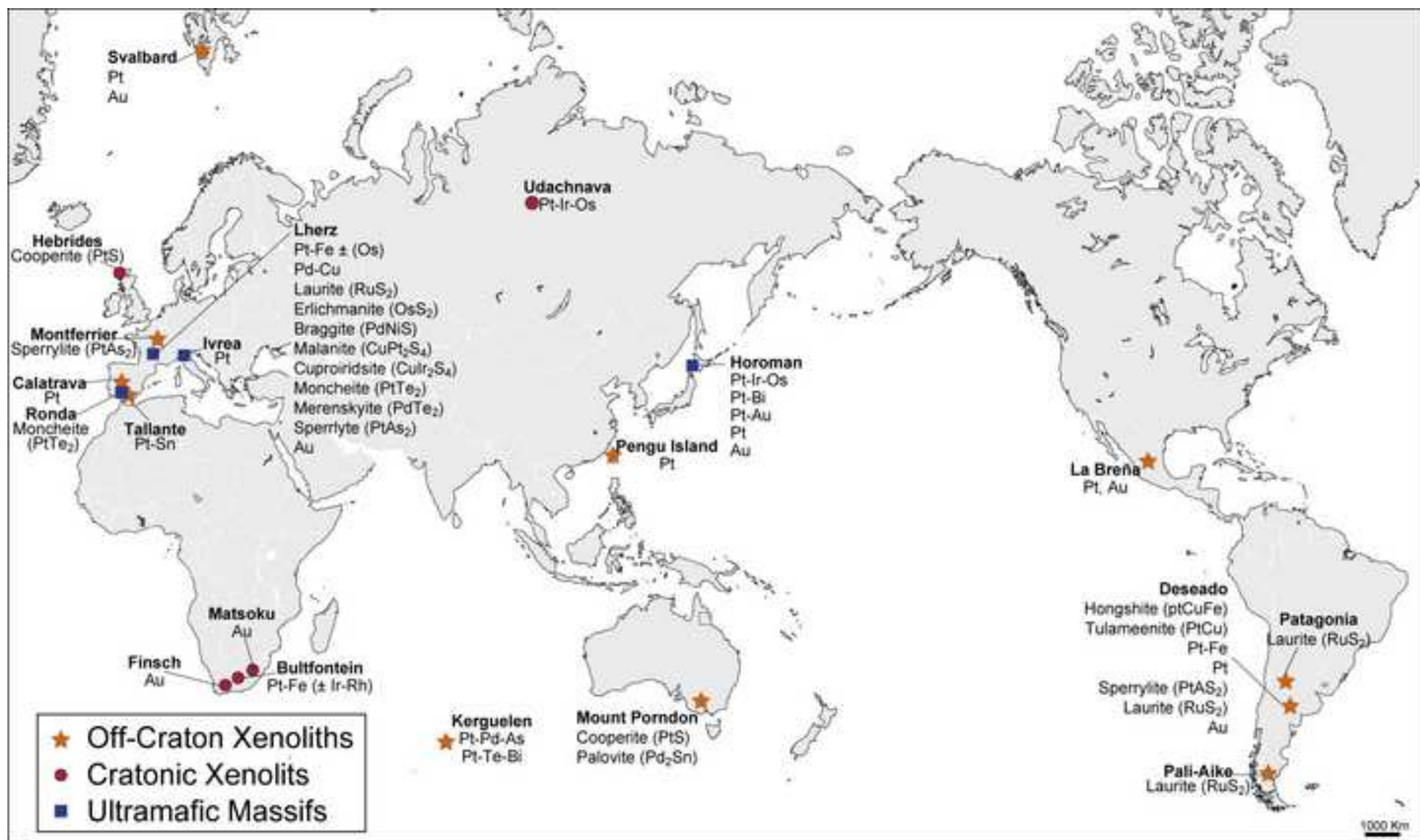


Figure 2
[Click here to download high resolution image](#)

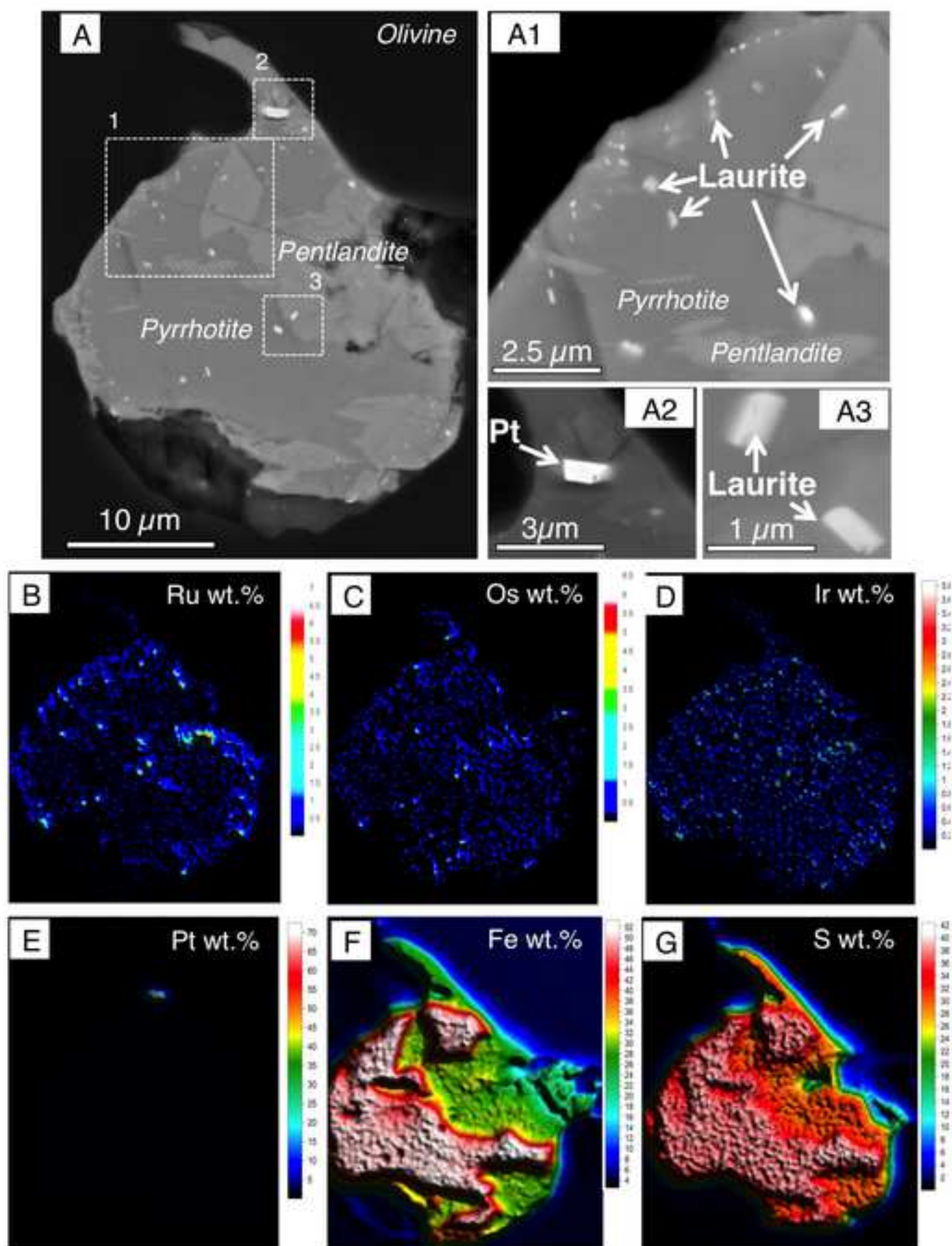


Figure 3
[Click here to download high resolution image](#)

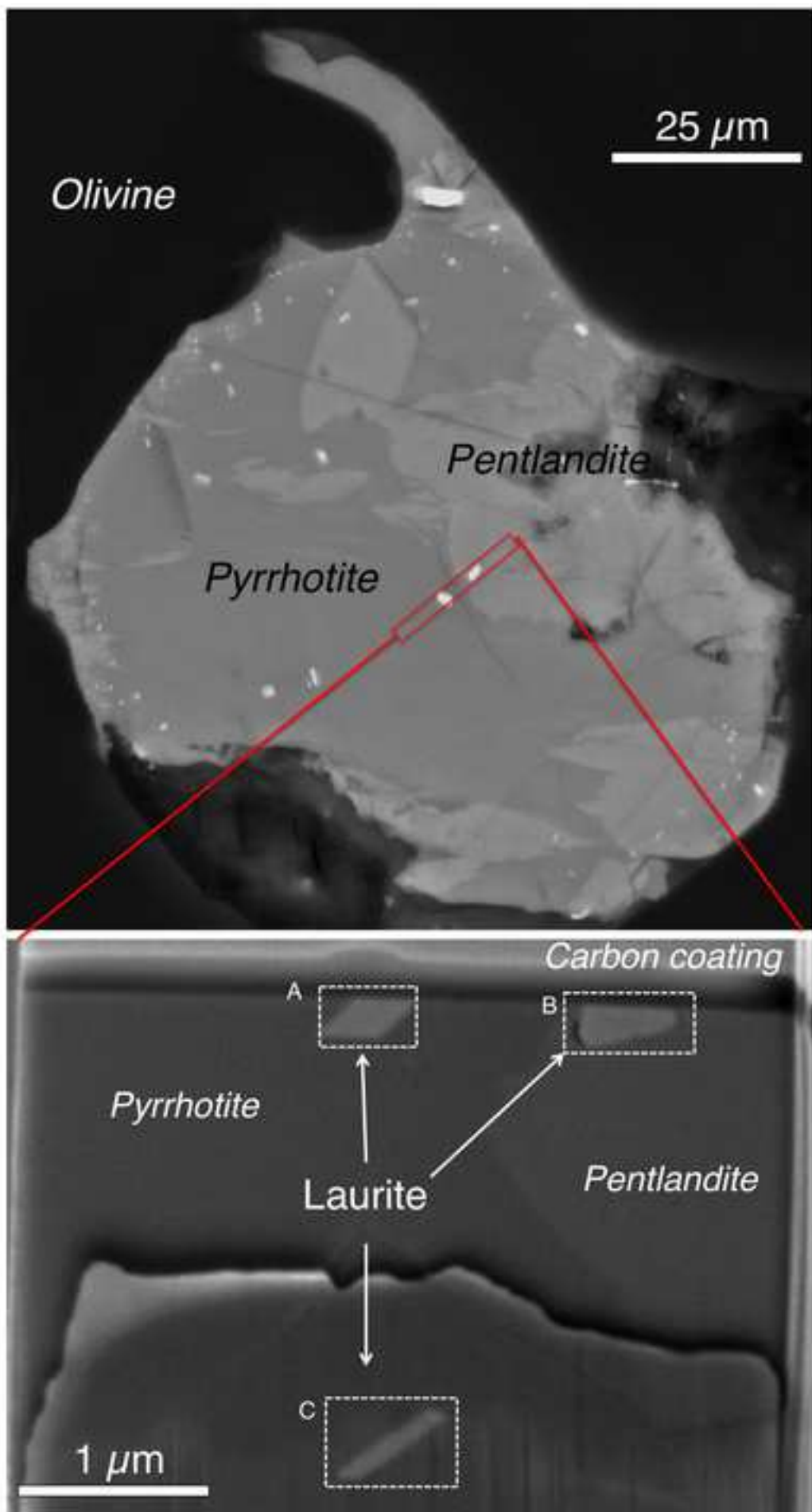


Figure 4
[Click here to download high resolution image](#)

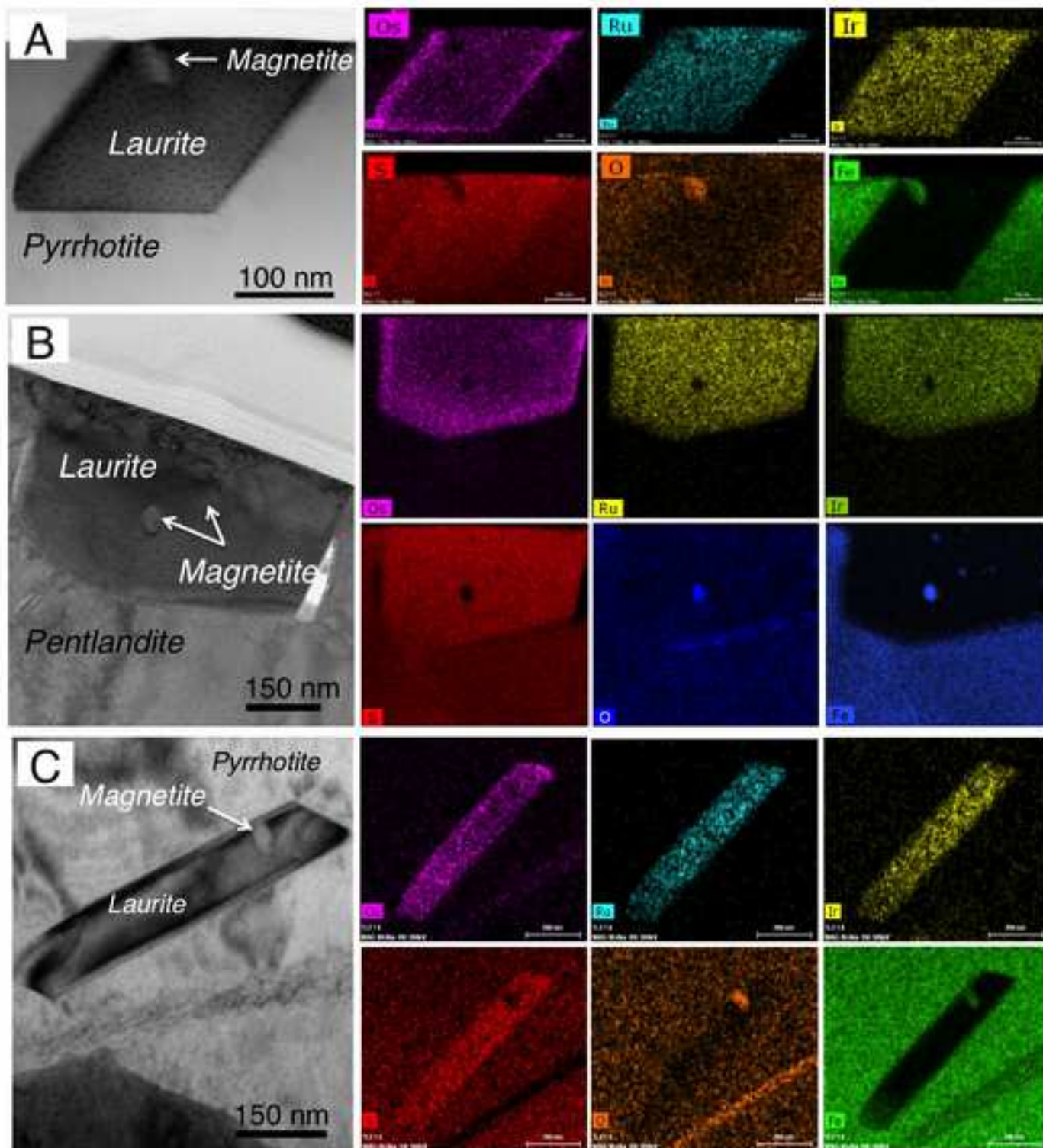


Figure 5
[Click here to download high resolution image](#)

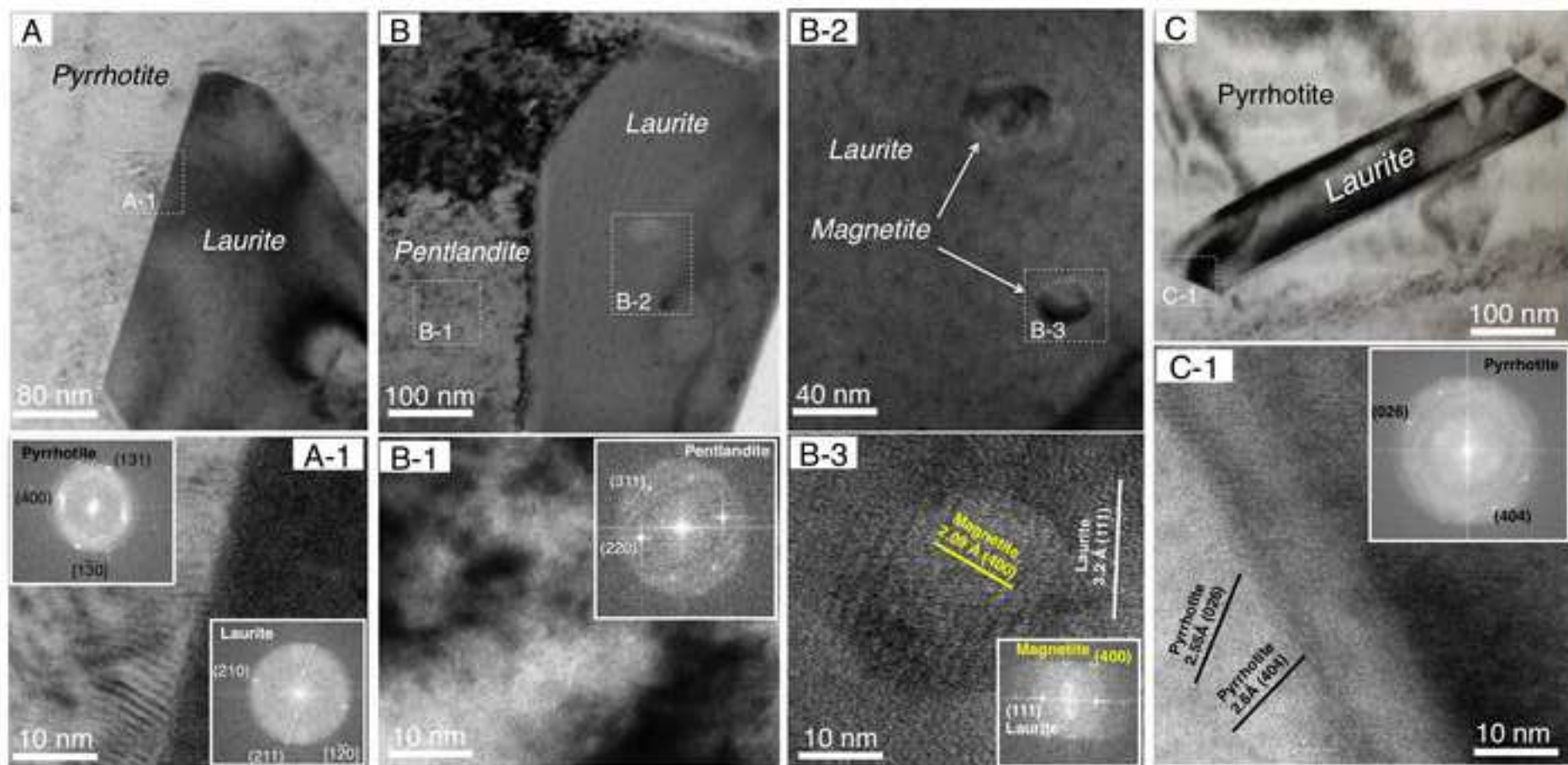


Figure 6
[Click here to download high resolution image](#)

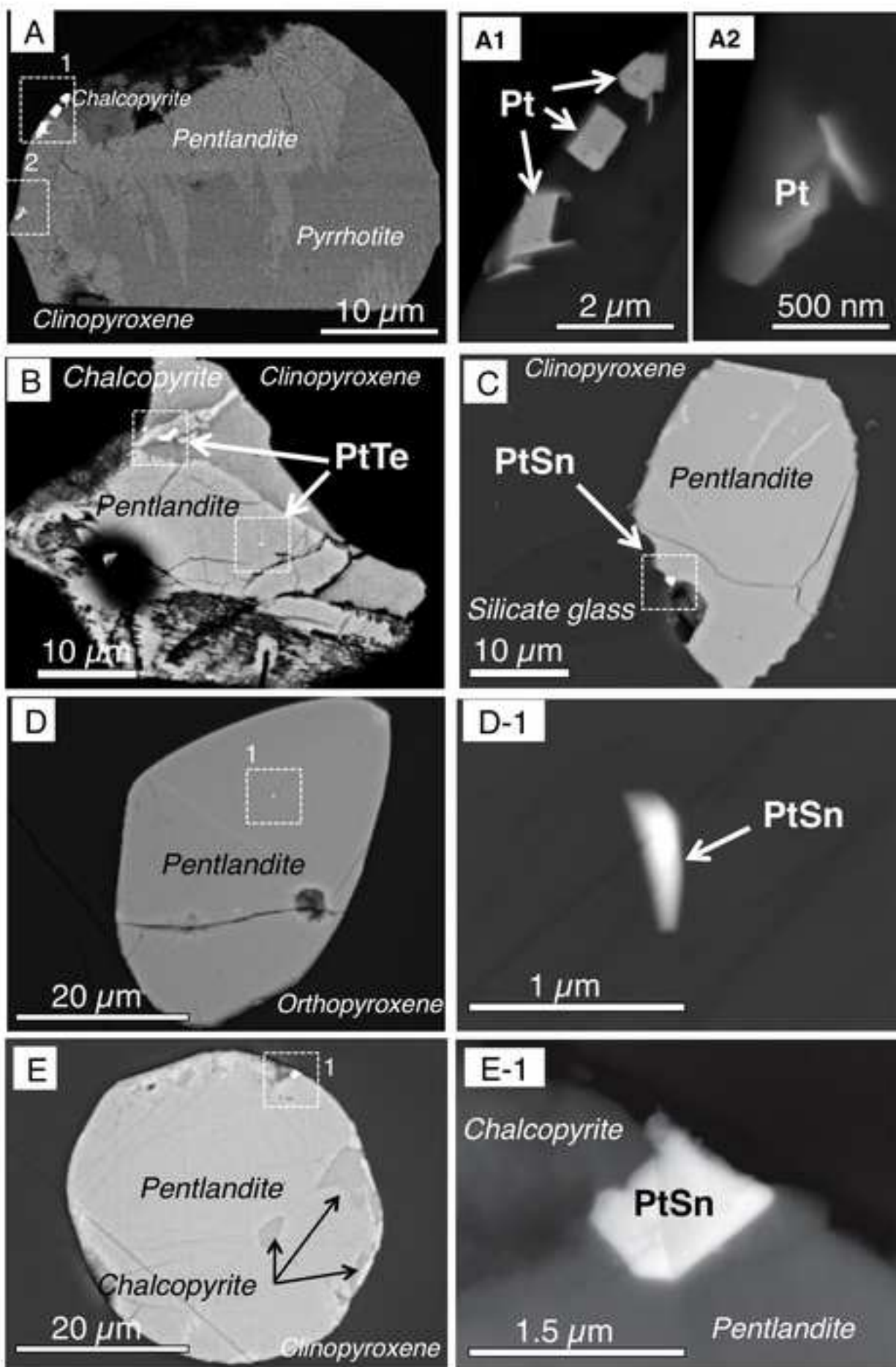


Figure 7

[Click here to download high resolution image](#)

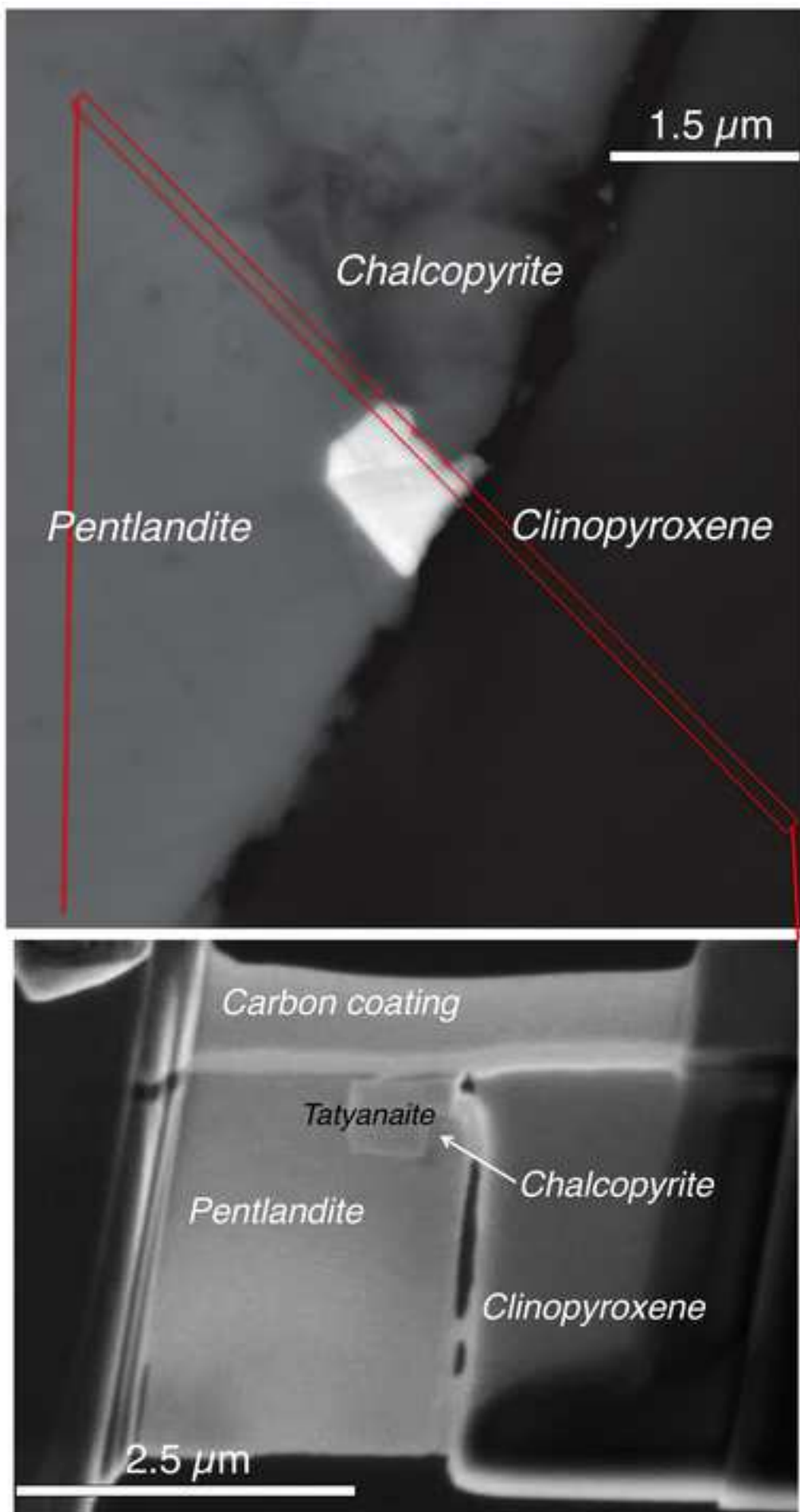


Figure 8
[Click here to download high resolution image](#)

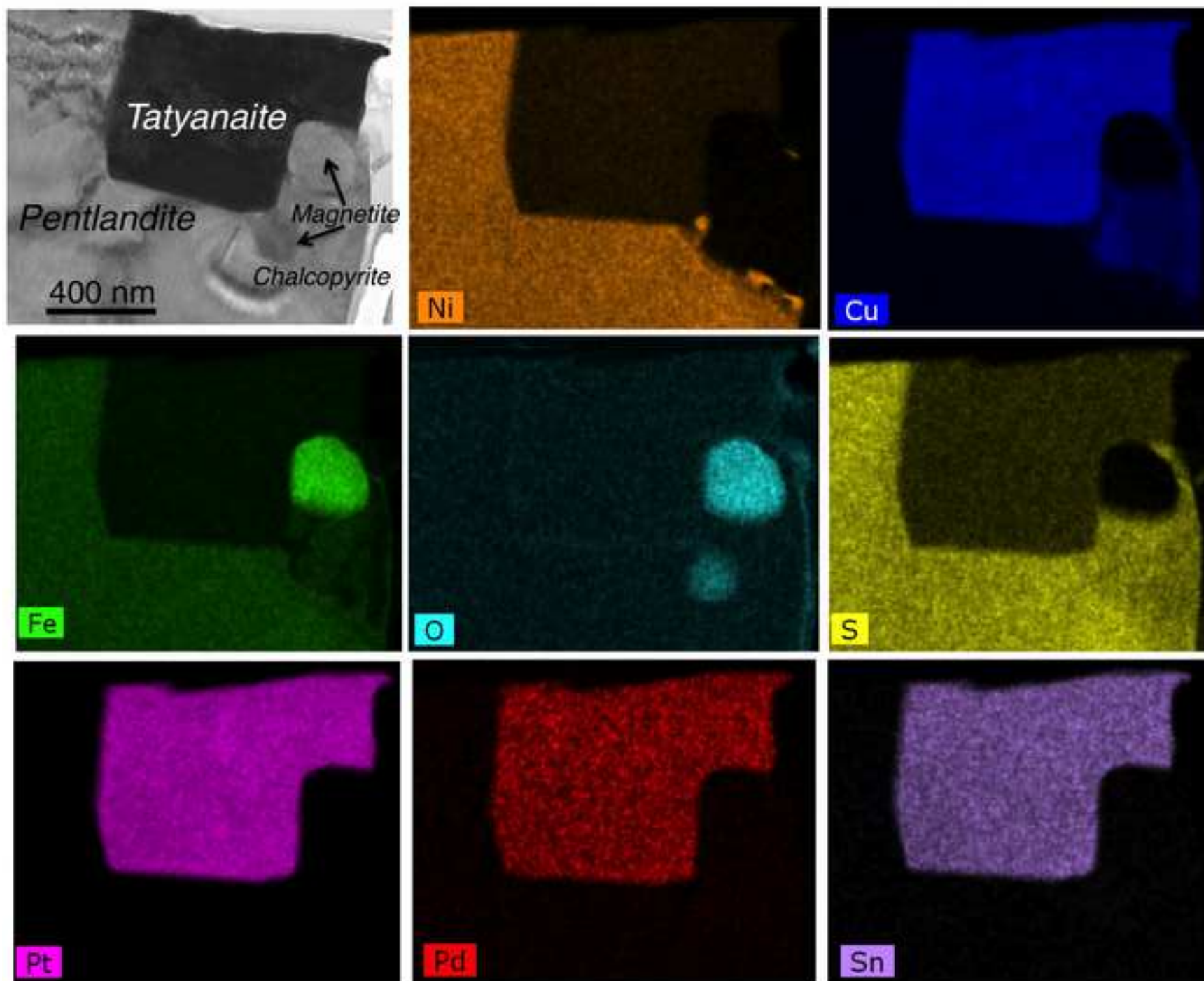


Figure 9
[Click here to download high resolution image](#)

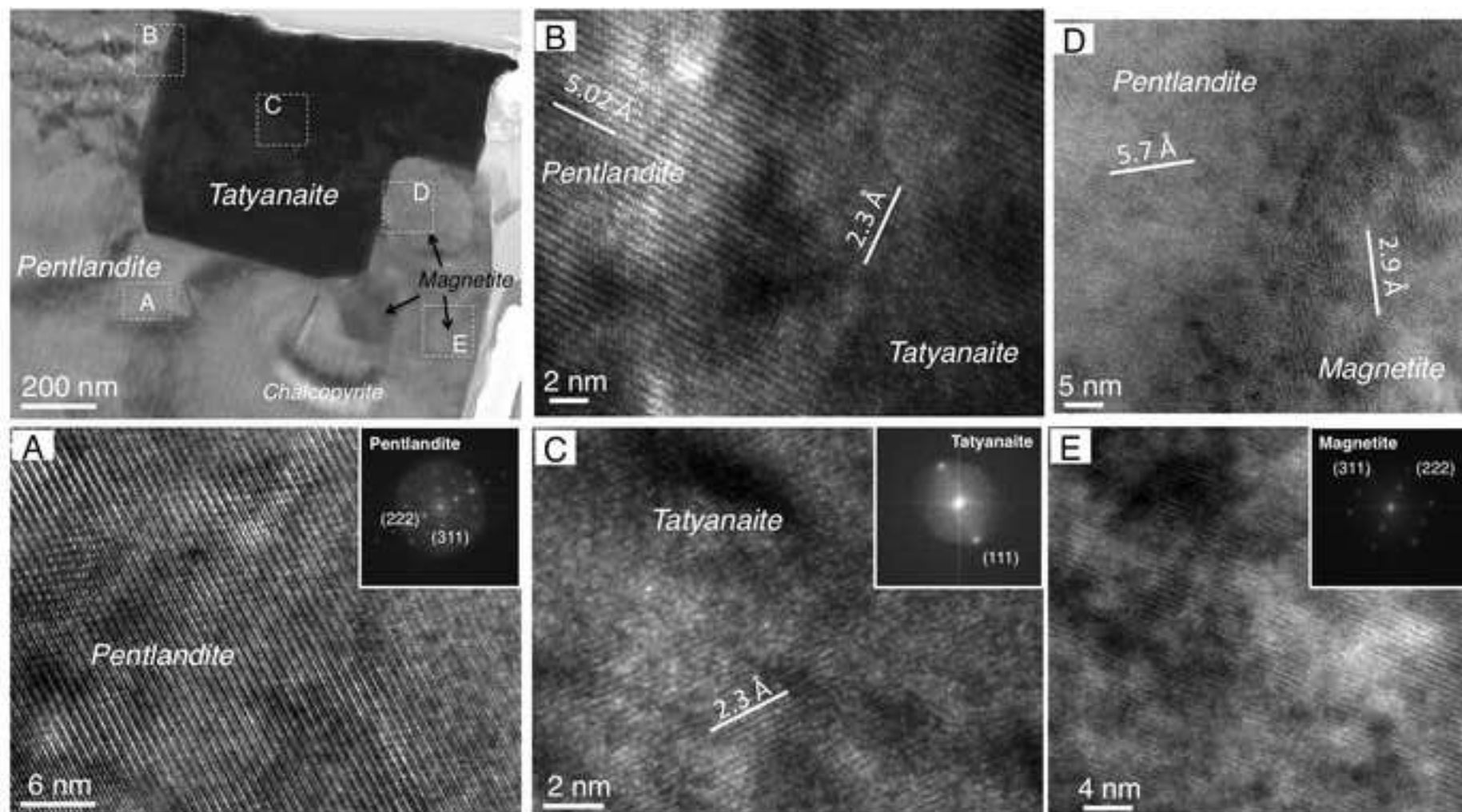


Figure 10

[Click here to download high resolution image](#)

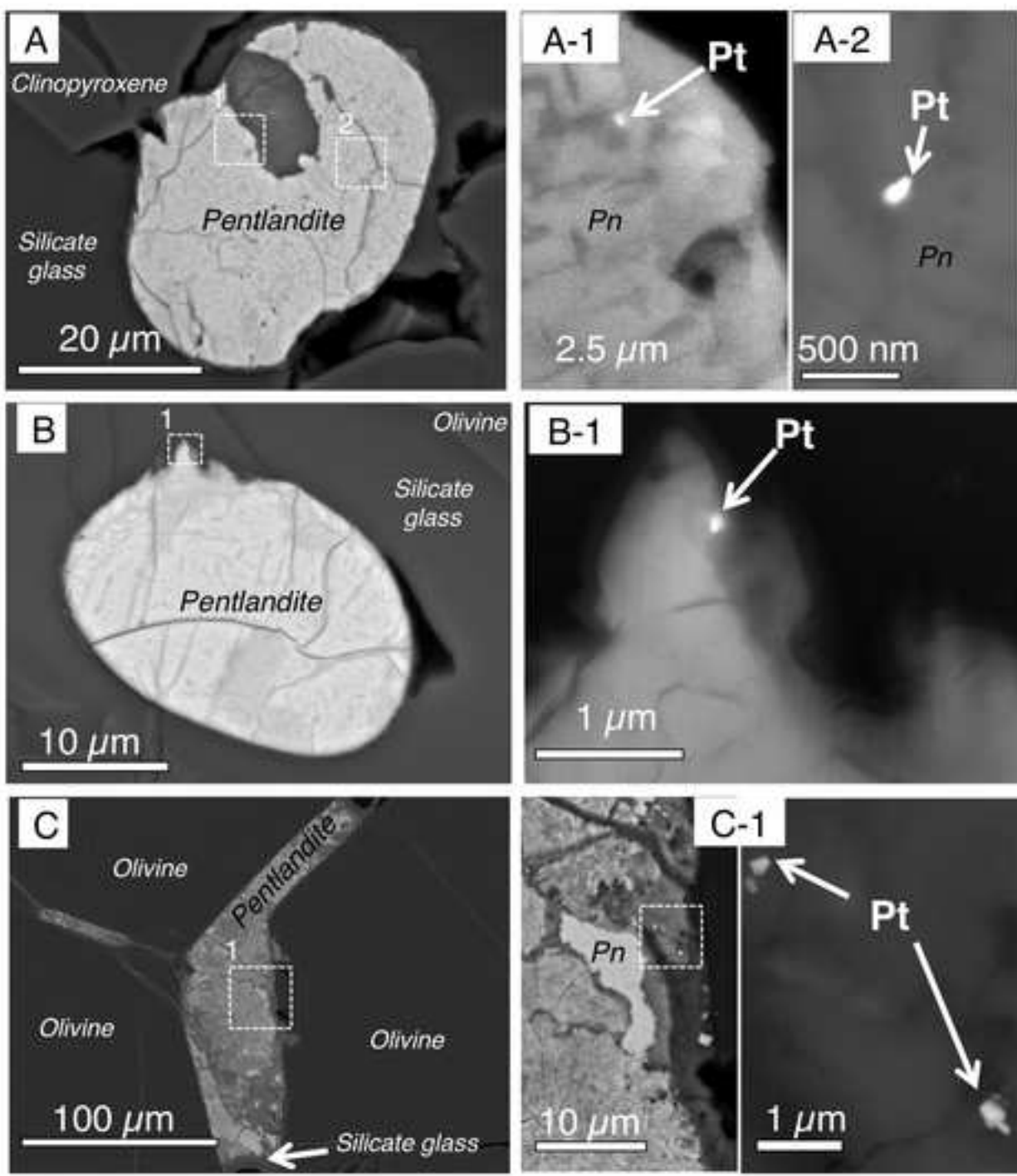


Figure 10

[Click here to download high resolution image](#)

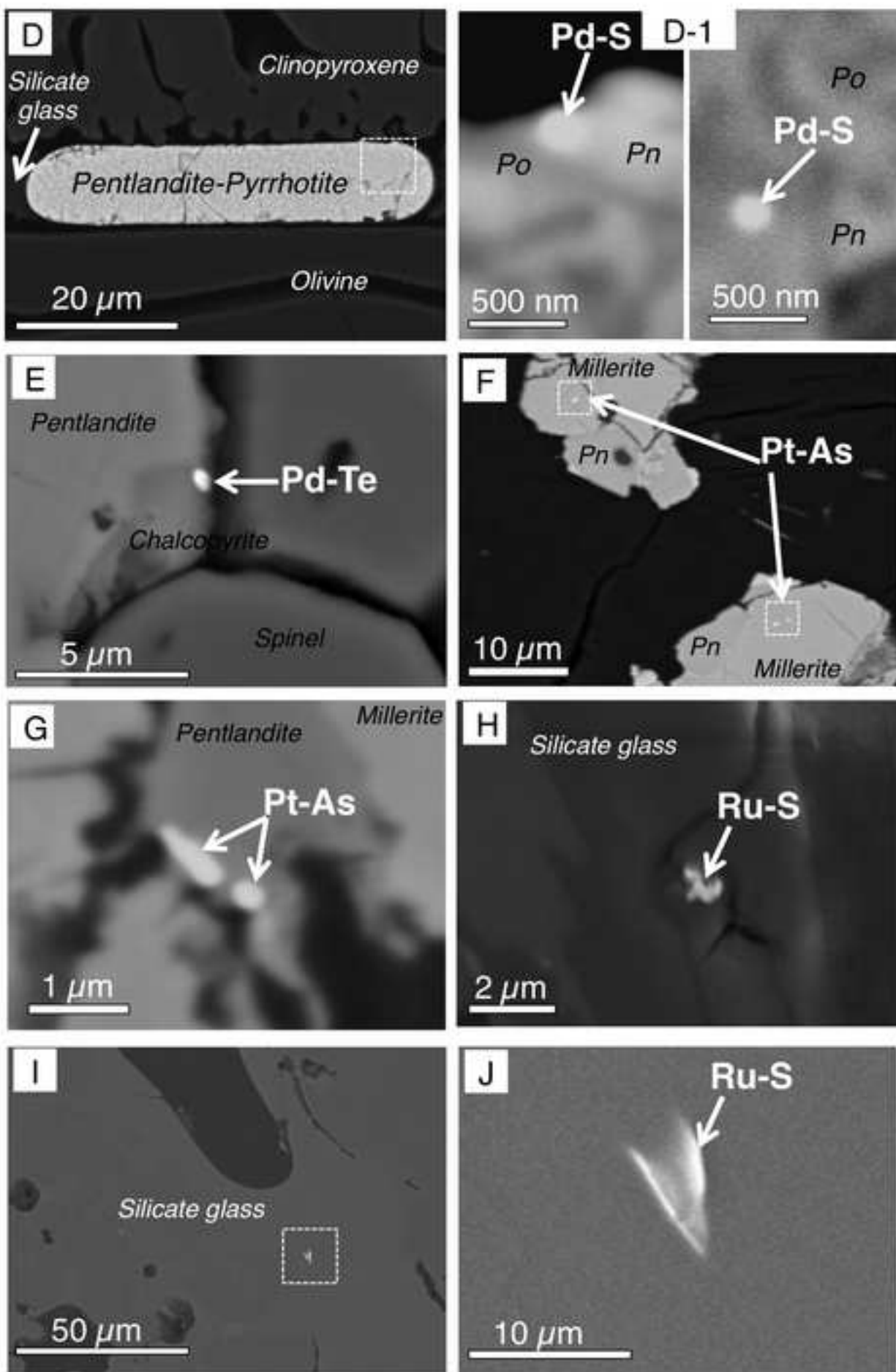


Figure 11

[Click here to download high resolution image](#)

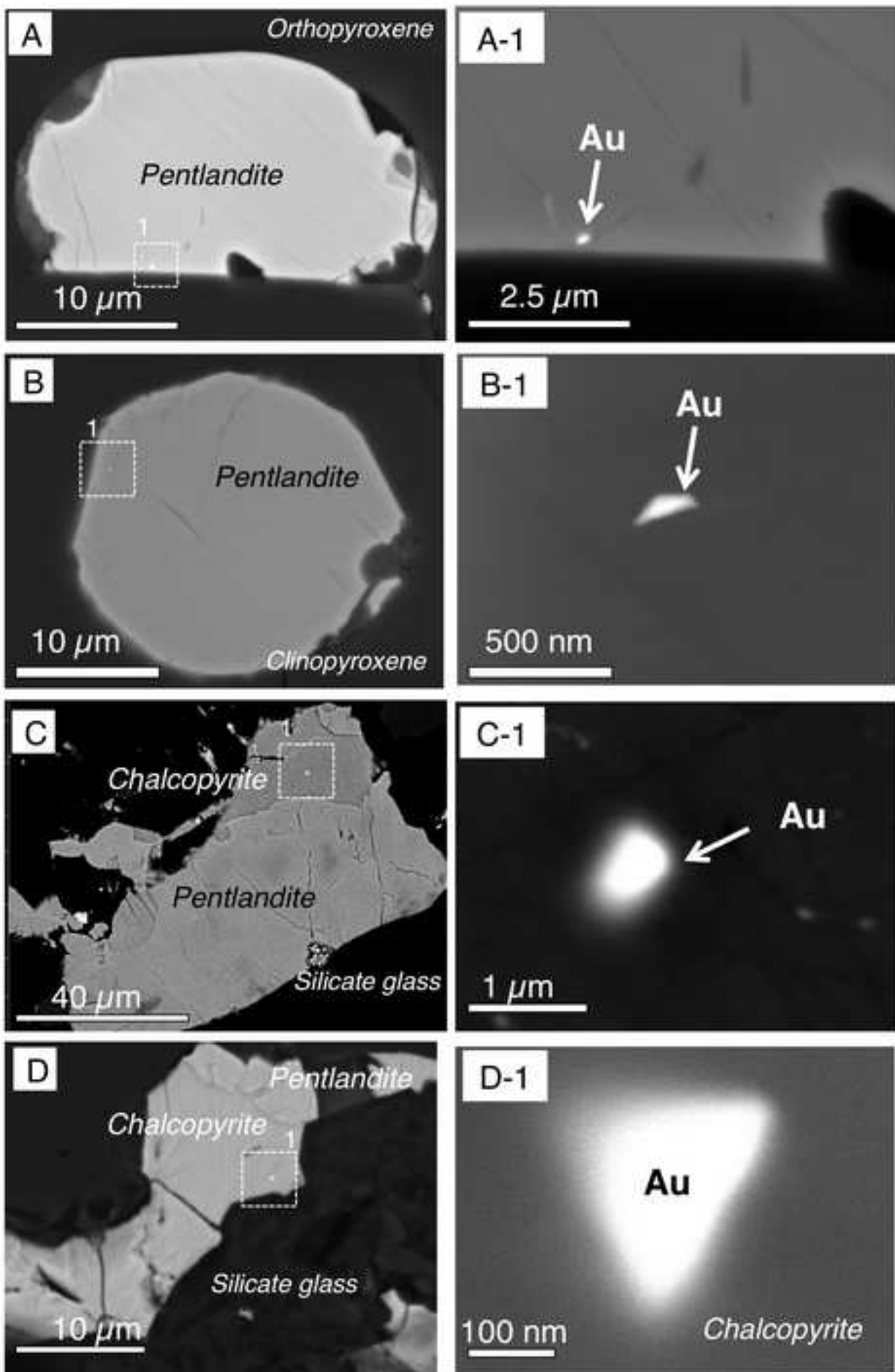


Figure 11

[Click here to download high resolution image](#)

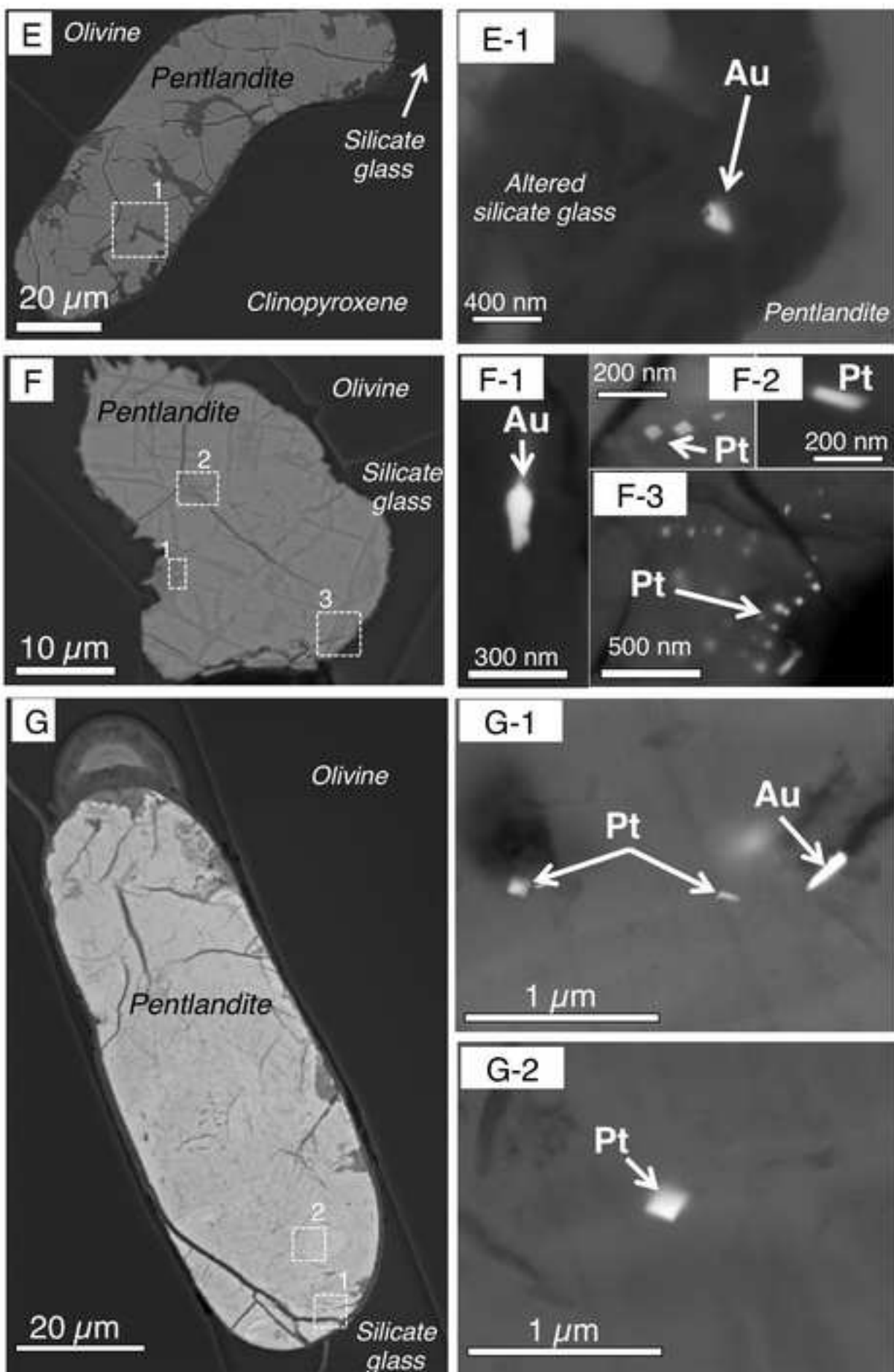
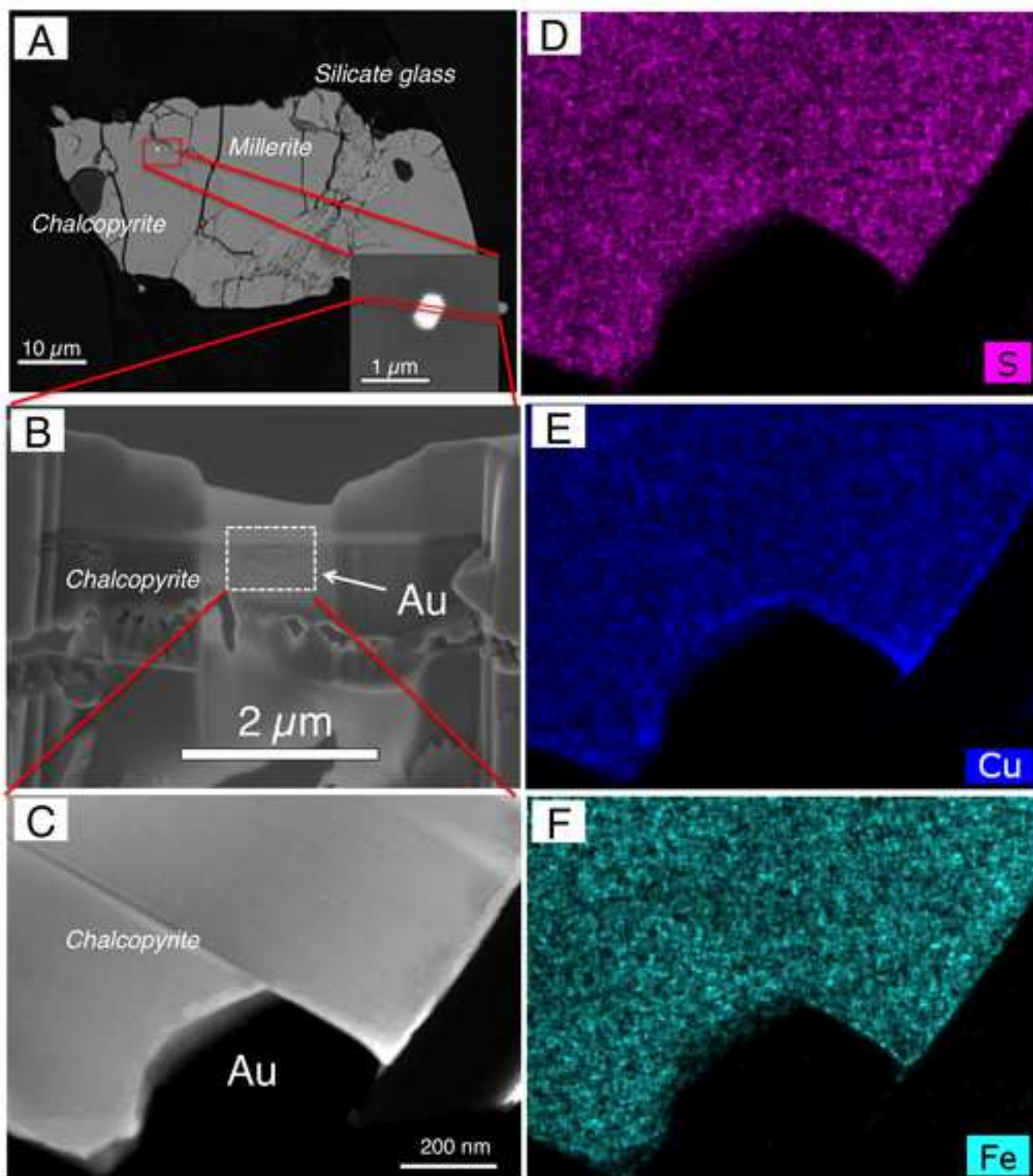


Figure 12
[Click here to download high resolution image](#)



Electronic Appendix 1

[Click here to download Supplementary material/Appendix \(Files for online publication only\): Appendix 1. Sample Localities.docx](#)

Electronic Appendix 2

[Click here to download Supplementary material/Appendix \(Files for online publication only\): Appendix 2. Analytical methods.do](#)

Electronic Appendix 3

[Click here to download Supplementary material/Appendix \(Files for online publication only\): Appendix 3_Chemical Composition](#)

Electronic Appendix 4

[Click here to download Supplementary material/Appendix \(Files for online publication only\): Appendix 4.EDS and EMPA analysis](#)

Electronic Appendix 5

[Click here to download Supplementary material/Appendix \(Files for online publication only\): Appendix 5. SAED Patterns.pdf](#)

Electronic Appendix 6

[Click here to download Supplementary material/Appendix \(Files for online publication only\): Appendix 6-LA-ICPMS time resolve](#)